Physical modelling of the slow voltage relaxation phenomenon in lithium-ion batteries

Toby L. Kirk[1,2], Colin P. Please[1,2], S. Jon Chapman[1,2]

[1]Mathematical Institute, University of Oxford, Andrew Wiles Building, Woodstock Road, Oxford, OX2 6GG, UK

[2]The Faraday Institution, Quad One, Becquerel Avenue, Harwell Campus, Didcot, OX11 0RA, UK

Abstract

In the lithium-ion battery literature, discharges followed by a relaxation to equilibrium are frequently used to validate models and their parametrizations. Good agreement with experiment during discharge is possible using a pseudo-two-dimensional model such as the Doyle-Fuller-Newman (DFN) model. The relaxation portion, however, is typically not well-reproduced, with the relaxation in experiments occurring much more slowly than in models. In this study, using a model that includes a size distribution of the active material particles, we give a physical explanation for the slow relaxation phenomenon. This model, the Many-Particle-DFN (MP-DFN), is compared against discharge and relaxation data from the literature, and optimal fits of the size distribution parameters (mean and variance), as well as solid-state diffusivities, are found using numerical optimization. The voltage after relaxation is captured by careful choice of the current cut-off time, allowing a single set of physical parameters to be used for all C-rates, in contrast to previous studies. We find that the MP-DFN can accurately reproduce the slow relaxation, across a range of C-rates, whereas the DFN cannot. Size distributions allow for greater internal heterogeneities, giving a natural origin of slower relaxation timescales that may be relevant in other, as yet explained, battery behavior.

1 Introduction

Lithium-ion batteries are rechargeable energy storage devices used across the consumer electronics industry due to their long lifespan, high energy density, and a low self-discharge rate compared to other batteries [1]. In recent years, their demand has grown due to their use in electric vehicles, and it is predicted to increase from 45 GWh per year in 2015 to 390

GWh per year by 2030 [2], motivating improvements in battery performance. Although experimental research is necessary to achieve this, mathematical modelling also plays a key role—for recent reviews of the various scales and complexities that have been modelled, see [3, 4]. The pioneering continuum model, still used today, was developed by the group of Newman [5, 6, 7, 8] where a macroscale (i.e., cell scale) model is coupled at each location to a microscale (i.e., particle scale) one—a picture justified by asymptotic homogenization [9], and also referred to as pseudo-two-dimensional (P2D).

A frequently occurring scenario, both in battery use and in research, is that of relaxation to equilibruim after a period of dynamic (dis)charging. During a (dis)charge, the internal state of the cell is transient with heterogeneities in lithium concentrations, in the electrolyte and the active materials of both the positive and negative electrodes. When the (dis)charge is stopped and the circuit current is switched off, the internal states then equilibriate and relax to a uniform steady state. This relaxation could take several hours, even 24 hours or longer [10], depending on the size of internal heterogeneities at current cut-off. There are two key components of this relaxation for a physical model to capture which are easily observed in experiments:

(i) The final equilibrium voltage after relaxation;

(ii) The manner or shape of the voltage relaxation profile.

Research on voltage relaxation has been focused mainly on improving the accuracy of open circuit voltage (OCV) measurements, typically done using the galvanostatic intermittent titration technique (GITT), where steps are taken through states of charge (SoC) incrementally, waiting for the cell to sufficiently relax after each step. The measurement of property (i) is then of importance, and strategies have been developed to measure this voltage accurately in a shorter time [11, 12, 13], achieved by fitting equivalent circuit models to (ii) with several (up to 5) RC elements, with large time constants that are difficult to interpret physically [11].

Battery relaxation has also found uses in the parametrization of physical models. These include recent comprehensive studies by Ecker et al. [14, 15], Schmalstieg et al. [16, 17], and Chen et al. [18], which use state-of-the-art experimental characterization techniques to parametrize (variants of) the Doyle-Fuller-Newman (DFN) model [5, 6] for commercial cells. The DFN is used across the lithium-ion battery literature and considered a benchmark. These studies use current pulses at a range of SoCs [14, 15, 16, 17], but also full discharges [14, 15, 16, 17, 18], each followed by relaxations, in order to validate their parametrizations and demonstrate the accuracy of their physical models. However, the slow relaxations of the experiments, clearly visible in [15] (Figs. 5, 6, 8), [17] (Figs. 6, 9), and [18] (Fig. 17), are not captured by the models, and are given minimal (if any) discussion. At low SoCs, the final rest voltage is also highly inaccurate, as seen in [15] (Fig. 6), [17] (Figs. 6, 9). Chen et al. [18] use the final rest voltage after a discharge to inform their parameter estimates, resulting in different parameter values needed for each experiment. This slow relaxation is not confined to lithium ion batteries but is also seen in other chemistries, e.g., lead acid where model parametrizations have faced similar difficulties [19].

In this paper, we will give a physical explanation for the slow relaxation phenomenon using an extension of the DFN to include a distribution of active particle sizes. Models with multiple (or distributions of) particle sizes have been considered by several authors, e.g. [20, 21, 22, 23], but not in the context of relaxation. In particular, the effects of particle-size distributions on discharge behaviour [20, 24, 23] and the imedpance response [21, 22] have been the main motivation in such studies. The model we use, denoted the Many-Particle-DFN (MP-DFN), is compared against the discharge and relaxation experimental data of [18], taken from a set of commercial cells (LG M50). The MP-DFN is initially parametrized by modifying the DFN parameter set in [18]; the process is described in sufficient detail to facilitate its use for other cells and chemistries. Simulations are performed using the open source software package Python Battery Mathematical Modelling (PyBaMM) [25] and optimal estimates of the microstructural parameters related to the size distributions (mean and variance), and solid-state diffusivities, are found by fitting the voltage profiles (across discharge and relaxation) using a numerical optimization package (DFO-LS [26]). We also present evidence that, for the cells considered here, the inclusion of particle-size distributions is more important for recovering the slow relaxation than employing a more physically realistic lithium transport model (nonlinear diffusion rather than Fickian diffusion) in the active material.

The structure of the paper is as follows. The mathematical models (MP-DFN and DFN), geometry and notation, are defined in section 2; the parameter set from the literature, and how it was adapted, is in section 3. The methodology is described in section 4, with the model comparisons (and parameter fitting) presented in section 5, followed by conclusions and future work.

2 Modelling

In this section, we describe the mathematical models considered in this paper, the MP-DFN and DFN. We first describe the geometry and notation used, then state the MP-DFN model as it is the most general, followed by the DFN which is a special case of the MP-DFN.

2.1 Geometry and notation

First, we summarise the geometry and notation used within both models. A schematic of the multiscale nature of the geometry is shown in Fig. 1.The macroscale geometry of the cell is one dimensional, with variation only in the through-cell direction, measured by the coordinate x. Thicknesses of the negative electrode, separator and positive electrode are L_{n}, L_{sep}, and L_{p}, respectively. The total thickness of the cell, from the negative current collector (at $x = 0$) to the positive current collector (at $x = L$) is thus $L = L_{\mathrm{n}} + L_{\mathrm{sep}} + L_{\mathrm{p}}$. The macroscale is divided into three regions,

$$\underset{\text{(negative electrode)}}{\Omega_{\mathrm{n}} = \{0 \leq x < L_{\mathrm{n}}\}}, \qquad \underset{\text{(separator)}}{\Omega_{\mathrm{sep}} = \{L_{\mathrm{n}} \leq x < L - L_{\mathrm{p}}\}}, \qquad \underset{\text{(positive electrode)}}{\Omega_{\mathrm{p}} = \{L - L_{\mathrm{p}} \leq x < L\}}, \tag{1}$$

At each macroscale location of both electrodes, $x \in \Omega_\mathrm{k}$, $\mathrm{k} = \mathrm{n}, \mathrm{p}$, there is a microscale domain $\Omega'_\mathrm{k} = \{R_{\mathrm{k,min}} \leq R_\mathrm{k} \leq R_{\mathrm{k,max}}\}$ comprising a collection of spherical particles of solid active material. The range of particle radii R_k that are present is modelled as a continuum, taking all positive values between $R_{\mathrm{k,min}}$ and $R_{\mathrm{k,max}}$ (which could be 0 and ∞), with the fraction of all particles of a given radius R_k given by the (normalised) particle-size distribution $f_{\mathrm{k},n}(R_\mathrm{k})$. However, it is more convenient to deal with the fraction of *surface area* contributed by particles of radius R_k, which we denote $f_{\mathrm{k},a}(R_\mathrm{k})$ and refer to as the area-weighted particle-size distribution (aPSD). Particle size can then be interpreted as a microscale dimension with variable R_k. In this paper we consider the particle-size distribution to be independent of macroscale location x, but one could consider a non-uniform spatial distribution by letting $f_{\mathrm{k},a}(R_\mathrm{k})$ (and also Ω'_k, $R_{\mathrm{k,min}}$, $R_{\mathrm{k,max}}$, etc.) depend on x.

All active particles of a given size (and at a given location) behave identically, and have a further internal domain $\Omega''_\mathrm{k}(R_\mathrm{k}) = \{0 \leq r_\mathrm{k} \leq R_\mathrm{k}\}$ described (due to spherical symmetry) by the radial coordinate r_k. Hence, each electrode consists of a hierarchy of three domains or dimensions[1],

$$\widehat{\Omega}_\mathrm{k} = \bigcup_{x \in \Omega_\mathrm{k}} \left[\bigcup_{R_\mathrm{k} \in \Omega'_\mathrm{k}} \Omega''_\mathrm{k}(R_\mathrm{k}) \right]. \tag{2}$$

We use the subscript $\mathrm{k} \in \{\mathrm{n}, \mathrm{sep}, \mathrm{p}\}$ to indicate in which subdomain that variable is defined. Then for that subdomain, the phase, either solid or electrolyte, is denoted by the additional subscript s or e, respectively. The variables in the model and their subdomains are

$$\text{Electrolyte phase}: \ \phi_{\mathrm{e,k}}, c_{\mathrm{e,k}}, i_{\mathrm{e,k}}, N_{\mathrm{e,k}} \qquad x \in \Omega_\mathrm{k},\ \mathrm{k} = \mathrm{n}, \mathrm{sep}, \mathrm{p} \tag{3}$$

$$\text{Solid phase}: \ \phi_{\mathrm{s,k}}, i_{\mathrm{s,k}} \qquad x \in \Omega_\mathrm{k},\ \mathrm{k} = \mathrm{n}, \mathrm{p} \tag{4}$$

$$c_{\mathrm{s,k}}, N_{\mathrm{s,k}} \qquad x \in \Omega_\mathrm{k},\ R_\mathrm{k} \in \Omega'_\mathrm{k},\ r_\mathrm{k} \in \Omega''_\mathrm{k}(R_\mathrm{k}),\ \mathrm{k} = \mathrm{n}, \mathrm{p} \tag{5}$$

where potentials are denoted by ϕ, current densities by i, molar lithium concentrations by c (with $c_{\mathrm{e,k}}$ being lithium-ion concentrations), and molar fluxes by N. We note that all quantities depend on the macroscale coordinate x and time t, but $c_{\mathrm{s,k}}$ (and $N_{\mathrm{s,k}}$) depend additionally on the microscale coordinates: particle radius $R_\mathrm{k} \in [R_{\mathrm{k,min}}, R_{\mathrm{k,max}}]$ and the radial coordinate $r_\mathrm{k} \in [0, R_\mathrm{k}]$. The parameters are described in Table 1, along with their values from the literature [18].

2.2 Many-Particle-Doyle-Fuller-Newman model (MP-DFN)

2.2.1 Dimensional governing equations

Charge conservation

The conservation of charge in the electrolyte and electrode phases is given by

[1]This means the model could be referred to as "pseudo-three-dimensional" or P3D, with particle size interpreted as another pseudo-dimension.

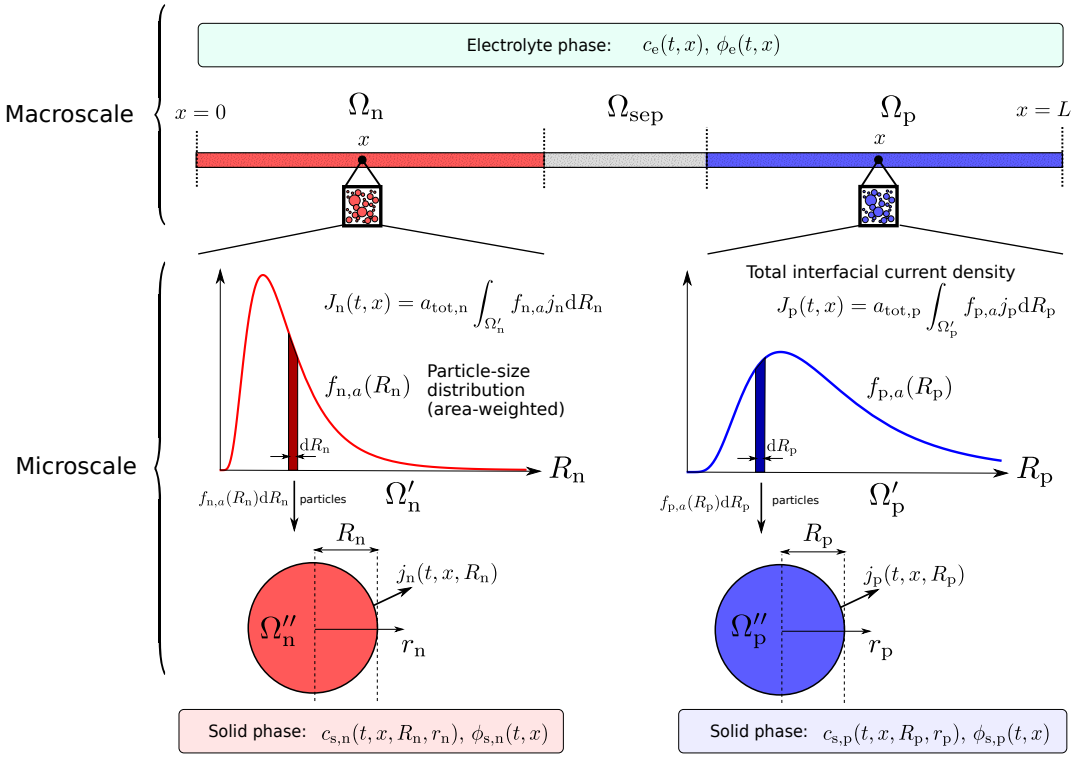

Figure 1: Schematic depicting the multi-scale geometry used for the Many-Particle-DFN model. The macroscale (x) and microscale dimensions (R_k, r_k for $k = n, p$), as well as the fundamental variables in the solid and electrolyte phases, are shown.

$$\frac{\partial i_{\mathrm{e,k}}}{\partial x} = -\frac{\partial i_{\mathrm{s,k}}}{\partial x} = \begin{cases} J_{\mathrm{k}}, & \mathrm{k} = \mathrm{n}, \mathrm{p}, \\ 0, & \mathrm{k} = \mathrm{sep}, \end{cases} \qquad \mathrm{k} \in \{\mathrm{n}, \mathrm{sep}, \mathrm{p}\}. \tag{6}$$

The interfacial current density J_{k} represents the total charge transfer, due to electrochemical reactions, between the active material and electrolyte at a given x location. The current densities in the electrolyte and electrode material are given by MacInnes' equation and Ohm's law, respectively,

$$i_{\mathrm{e,k}} = \epsilon_{\mathrm{k}}^{b_{\mathrm{k}}} \kappa_{\mathrm{e}}(c_{\mathrm{e,k}}) \left[-\frac{\partial \phi_{\mathrm{e,k}}}{\partial x} + 2(1-t^+) \frac{R_g T}{F} \frac{\partial}{\partial x} \log c_{\mathrm{e,k}} \right], \qquad \mathrm{k} \in \{\mathrm{n}, \mathrm{sep}, \mathrm{p}\}, \tag{7}$$

$$i_{\mathrm{s,k}} = -\sigma_{\mathrm{k}} \frac{\partial \phi_{\mathrm{s,k}}}{\partial x}, \qquad \mathrm{k} \in \{\mathrm{n}, \mathrm{p}\}. \tag{8}$$

There is continuity of $i_{\mathrm{e,k}}, \phi_{\mathrm{e,k}}$ and $i_{\mathrm{s,k}} = 0$ at the internal electrode/separator boundaries, $x = L_{\mathrm{n}}, L - L_{\mathrm{p}}$. At the current collectors, charge only enters/exits the cell via the solid phase, with current density $i_{\mathrm{s,n}} = i_{\mathrm{app}}$ (time-dependent, in general) imposed at $x = 0$, but also $i_{\mathrm{s,p}} = i_{\mathrm{app}}$ at $x = L$ by conservation of charge:

$$i_{\mathrm{e,k}} = 0, \qquad \text{at } x = 0, L \tag{9}$$

$$i_{\mathrm{s,k}} = i_{\mathrm{app}}(t), \qquad \text{at } x = 0, L \tag{10}$$

Then the solid-phase potentials at the current collectors are

$$\phi_{\mathrm{s,n}} = 0 \quad \text{at } x = 0, \qquad\qquad \phi_{\mathrm{s,p}} = V \quad \text{at } x = L. \tag{11}$$

Adding the $i_{\mathrm{e,k}}$ and $i_{\mathrm{s,k}}$ equations in (6), integrating over each region and imposing continuity gives that $i_{\mathrm{s,k}} + i_{\mathrm{e,k}} = i_{\mathrm{app}}$ in each electrode which can be used to eliminate $i_{\mathrm{s,k}}$, and in the separator,

$$i_{\mathrm{e,sep}} \equiv i_{\mathrm{app}}. \tag{12}$$

Molar conservation of lithium

In the electrolyte:

$$\epsilon_{\mathrm{k}} \frac{\partial c_{\mathrm{e,k}}}{\partial t} = -\frac{\partial N_{\mathrm{e,k}}}{\partial x} + \frac{1}{F} \frac{\partial i_{\mathrm{e,k}}}{\partial x}, \quad \mathrm{k} \in \{\mathrm{n}, \mathrm{sep}, \mathrm{p}\}, \tag{13}$$

$$N_{\mathrm{e,k}} = -\epsilon_{\mathrm{k}}^{b_{\mathrm{k}}} D_{\mathrm{e}}(c_{\mathrm{e,k}}) \frac{\partial c_{\mathrm{e,k}}}{\partial x} + \frac{t^+}{F} i_{\mathrm{e,k}}, \quad \mathrm{k} \in \{\mathrm{n}, \mathrm{sep}, \mathrm{p}\}, \tag{14}$$

with continuity of $c_{\mathrm{e,k}}, N_{\mathrm{e,k}}$ at internal boundaries $x = L_{\mathrm{n}}, L - L_{\mathrm{p}}$, and no-flux $N_{\mathrm{e,k}} = 0$ at the current collectors $x = 0, L$.

In the active solid electrode particles, lithium transport is modelled by Fickian diffusion (except in section 5.3 where nonlinear diffusion is considered),

$$\frac{\partial c_{\mathrm{s,k}}}{\partial t} = -\frac{1}{r_{\mathrm{k}}^2}\frac{\partial}{\partial r_{\mathrm{k}}}(r_{\mathrm{k}}^2 N_{\mathrm{s,k}}), \quad \mathrm{k} \in \{\mathrm{n}, \mathrm{p}\}, \tag{15}$$

$$N_{\mathrm{s,k}} = -D_{\mathrm{s,k}}\frac{\partial c_{\mathrm{s,k}}}{\partial r_{\mathrm{k}}}, \quad \mathrm{k} \in \{\mathrm{n}, \mathrm{p}\}, \tag{16}$$

with regularity at the particle centres, and a flux condition at the surface,

$$N_{\mathrm{s,k}} = 0, \quad \text{at } r_{\mathrm{k}} = 0, \qquad\qquad N_{\mathrm{s,k}} = \frac{j_{\mathrm{k}}}{F}, \quad \text{at } r_{\mathrm{k}} = R_{\mathrm{k}}, \tag{17}$$

where j_{k} is the interfacial current density representing the charge transfer into the electrolyte, which may be different for particles of different sizes. The total interfacial current density originating from all particles at that macroscale location x is then

$$J_{\mathrm{k}} = \int_{\Omega'_{\mathrm{k}}} a_{\mathrm{k}}(R_{\mathrm{k}}) j_{\mathrm{k}} \,\mathrm{d}R_{\mathrm{k}} = a_{\mathrm{tot,k}} \int_{\Omega'_{\mathrm{k}}} f_{\mathrm{k},a}(R_{\mathrm{k}}) j_{\mathrm{k}} \,\mathrm{d}R_{\mathrm{k}} \tag{18}$$

which appears as a charge source/sink in (6), and a lithium-ion source/sink in (13). The total active surface area per unit volume, $a_{\mathrm{tot,k}}$, is determined from the volume fraction of active material, $\epsilon_{s,\mathrm{k}}$, and the distribution $f_{\mathrm{k},a}$ [23]

$$a_{\mathrm{tot,k}} = \frac{3\epsilon_{\mathrm{s,k}}}{\int_{\Omega'_{\mathrm{k}}} R_{\mathrm{k}} f_{\mathrm{k},a}(R_{\mathrm{k}}) \,\mathrm{d}R_{\mathrm{k}}} = \frac{3\epsilon_{\mathrm{s,k}}}{\bar{R}_{\mathrm{k},a}}, \tag{19}$$

where the factor of 3 is due to the assumption here of spherical particles. The radius $\bar{R}_{\mathrm{k},a}$ is the area-weighted mean radius, or the mean of $f_{\mathrm{k},a}(R_{\mathrm{k}})$—see section 3.1 for further discussion of aPSD quantities and their relevance.

Electrochemical reactions

The interfacial current density originating from the lithium (de)intercalation reaction on the surface ($r_{\mathrm{k}} = R_{\mathrm{k}}$) of all active particles in each electrode is modelled by symmetric Butler–Volmer kinetics (transfer coefficients equal to 1/2):

$$j_{\mathrm{k}} = j_{\mathrm{k},0} \sinh\left(\frac{F\eta_{\mathrm{k}}}{2R_g T}\right), \qquad \mathrm{k} \in \{\mathrm{n}, \mathrm{p}\}, \tag{20}$$

$$\text{Exchange current density}: \; j_{0,\mathrm{k}} = m_{\mathrm{k}}(c_{\mathrm{s,k}})^{1/2}(c_{\mathrm{k,max}} - c_{\mathrm{s,k}})^{1/2}(c_{\mathrm{e,k}})^{1/2}, \qquad \mathrm{k} \in \{\mathrm{n}, \mathrm{p}\}, \tag{21}$$

$$\text{Reaction overpotential}: \; \eta_{\mathrm{k}} = \phi_{\mathrm{s,k}} - \phi_{\mathrm{e,k}} - U_{\mathrm{k}}(c_{\mathrm{s,k}}), \qquad \mathrm{k} \in \{\mathrm{n}, \mathrm{p}\}, \tag{22}$$

In the above it is implicit that the concentration $c_{\mathrm{s,k}}$ is evaluated on the particle surface $r_{\mathrm{k}} = R_{\mathrm{k}}$.

Initial conditions

Initially, at $t = 0$, we take the cell to be at rest with all variables constant and uniform in space. The initial conditions are

$$c_{\mathrm{s,k}} = c_{\mathrm{k},0}, \qquad \mathrm{k} \in \{\mathrm{n}, \mathrm{p}\}, \tag{23}$$

$$c_{\mathrm{e,k}} = c_{\mathrm{e},0}, \qquad \mathrm{k} \in \{\mathrm{n}, \mathrm{sep}, \mathrm{p}\}, \tag{24}$$

which forces the initial potentials to be

$$U_{\mathrm{k}} = U_{\mathrm{k}}(c_{\mathrm{k},0}) = U_{\mathrm{k},0}, \qquad \mathrm{k} \in \{\mathrm{n}, \mathrm{p}\}, \tag{25}$$

$$\phi_{\mathrm{s,k}} = \begin{cases} 0, & \mathrm{k} = \mathrm{n}, \\ U_{\mathrm{p},0} - U_{\mathrm{n},0} & \mathrm{k} = \mathrm{p}, \end{cases} \tag{26}$$

$$\phi_{\mathrm{e,k}} = -U_{\mathrm{n},0}, \qquad \mathrm{k} \in \{\mathrm{n}, \mathrm{sep}, \mathrm{p}\}, \tag{27}$$

and all other variables are initially equal to zero.

2.3 Doyle-Fuller-Newman model

Here we state the standard Doyle-Fuller-Newman (DFN) model, the most commonly used physical porous electrode model of a lithium-ion cell, and the model employed in Chen et al. [18]. If we set all the particles in electrode k to be the same size, $R_{\mathrm{k}} = R_{\mathrm{k},DFN}$, then the aPSD is a Dirac delta function, $f_{\mathrm{k},a}(R_{\mathrm{k}}) = \delta(R_{\mathrm{k}} - R_{\mathrm{k},DFN})$, and the MP-DFN model reduces to the DFN model, with equation (18) reducing to $J_{\mathrm{k}} = a_{\mathrm{k}} j_{\mathrm{k}}|_{R_{\mathrm{k}} = R_{\mathrm{k},DFN}}$. Then, only the dynamics of particles of size $R_{\mathrm{k}} = R_{\mathrm{k},DFN}$ need to be modelled, and hence all of the remaining equations are identical to that of the MP-DFN, but with all variables (where applicable) evaluated at $R_{\mathrm{k}} = R_{\mathrm{k},DFN}$.

3 Parameter values from the literature

In order to later compare to the experimental results of Chen et al. [18] we use a parameter set based on their extensive parametrization of a cylindrical 21700 commercial cell (LGM50), tailored to their P2D model. The model in Chen et al. [18] is identical to the DFN, given in section 2 up to differences in notation. However, as the DFN assumes only a single particle size for each electrode, several modifications or additions to the parameter set are needed before its use with the MP-DFN, which we now detail.

3.1 Microscale parameters

The MP-DFN requires not only a mean or representative particle radius for each electrode, but a particle-size distribution. Particle-size distributions were measured in Chen et al. [18] using scanning electron microscopy (SEM) images of electrode cross-sections and grouping

Dimensional parameter	Description [unit]	Value, region k			Ref.
		n	sep	p	
ϵ_{k}	Electrolyte volume fraction	0.25	0.47	0.335	
b_{k}	Bruggeman coefficient	1.5	1.5	1.5	
L_{k}	Electrode thickness [m]	85.2×10^{-6}	12×10^{-6}	75.6×10^{-6}	
$\epsilon_{\mathrm{s,k}}$	Active material volume fraction	0.75	-	0.665	[18]
σ_{k}	Conductivity in in electrode material [S m^{-1}]	215	-	0.18	
$c_{\mathrm{k,max}}$	Max. Li concentration in active material [mol m^{-3}]	33133	-	63104	
$c_{\mathrm{k},0}$	Initial Li concentration in active material [mol m^{-3}]	29866	-	17038	
$U_{\mathrm{k}}(c_{s,\mathrm{k}})$	Open circuit potential relative to $\mathrm{Li/Li^+}$ [V]	Eq. (34)	-	Eq. (35)	
m_{k}	Reaction rate [A $\mathrm{m}^{-2}(\mathrm{m}^3/\mathrm{mol})^{1.5}$]	8.053×10^{-7}	-	4.443×10^{-6}	
$D_{\mathrm{s,k}}$	Diffusivity of Li in electrode [$\mathrm{m^2 s^{-1}}$]	5.10×10^{-14}	-	6.75×10^{-15}	Modified from [18]
$f_{\mathrm{k},a}(R_{\mathrm{k}})$	Area-weighted particle-size distribution (aPSD) [m^{-1}]	Eq. (30)	-	Eq. (30)	
$\bar{R}_{\mathrm{k},a}$	Area-weighted mean particle radius [m]	7.28×10^{-6}	-	6.78×10^{-6}	
$\sigma_{\mathrm{k},a}$	Area-weighted particle-size standard deviation [m]	2.08×10^{-6}	-	2.59×10^{-6}	
$a_{\mathrm{tot,k}}$	Total active surface area per volume from (19) [m^{-1}]	3.09×10^5	-	2.94×10^5	
$c_{\mathrm{e},0}$	Initial Li concentration in electrolyte [mol m^{-3}]	1000			
$D_{\mathrm{e,typ}}$	Typical diffusivity of lithium ions in electrolyte [$\mathrm{m^2 s^{-1}}$]	1.77×10^{-10}			
$\kappa_{\mathrm{e,typ}}$	Typical conductivity of electrolyte [S m^{-1}]	0.949			[18]
t^+	Cation transference number	0.2594			
R_g	Universal gas constant [J $\mathrm{mol^{-1} K^{-1}}$]	8.3145			
F	Faraday's constant [$\mathrm{Cmol^{-1}}$]	96485			
T	Temperature [K]	298.15			
C	Reference current density to discharge in 1hr [$\mathrm{Am^{-2}}$]	5			

Table 1: Dimensional parameters for use with the MP-DFN and DFN models, from Chen et al. [18], with modified or new parameters indicated—see section 3. Initial guesses used for the fitting of section 5.

the particles of similar sizes to produce histograms with bin widths of 1 μm (NMC 811 and graphite) or 0.5 μm (SiO_x). This amounts to a (discrete) estimate of the number density $n_{\mathrm{k}}(R_{\mathrm{k}})$, i.e., the number of particles of size R_{k} per unit volume in electrode k. It is more convenient, but also more physically relevant due to the interfacial nature of the electrochemical reactions (see [23]), to work in terms of the area density $a_{\mathrm{k}}(R_{\mathrm{k}}) = 4\pi R_{\mathrm{k}}^2 n_{\mathrm{k}}(R_{\mathrm{k}})$, or its normalised version, the area-weighted particle-size distribution (aPSD),

$$f_{\mathrm{k},a}(R_{\mathrm{k}}) = \frac{a_{\mathrm{k}}(R_{\mathrm{k}})}{\int_{\Omega'_{\mathrm{k}}} a_{\mathrm{k}}(R_{\mathrm{k}})\,\mathrm{d}R_{\mathrm{k}}} = \frac{a_{\mathrm{k}}(R_{\mathrm{k}})}{a_{\mathrm{tot,k}}} \tag{28}$$

$$= \frac{R_{\mathrm{k}}^2 n_{\mathrm{k}}(R_{\mathrm{k}})}{\int_{\Omega'_{\mathrm{k}}} R_{\mathrm{k}}^2 n_{\mathrm{k}}(R_{\mathrm{k}})\,\mathrm{d}R_{\mathrm{k}}}. \tag{29}$$

For the MP-DFN, it is sufficient to specify the function $a_{\mathrm{k}}(R_{\mathrm{k}})$, which we achieve by specifying its integral, $a_{\mathrm{tot,k}}$, and its shape, $f_{\mathrm{k},a}(R_{\mathrm{k}})$ (which integrates to one). Here we convert the measurements of $n_{\mathrm{k}}(R_{\mathrm{k}})$ in Chen et al. [18] to a discrete area-weighted (and normalised) distribution using (29), and then fit a continuous density function $f_{\mathrm{k},a}(R_{\mathrm{k}})$. The distribution data is shown in Fig. 2 for the positive electrode (NMC) and negative electrode (graphite, with the small contributions of SiO_x neglected). The distributions are unimodal with positive skew, motivating their representation by a lognormal—commonly used for electrode PSDs [21, 22, 23]—given by

$$f_{\mathrm{k},a}(R) = \frac{1}{R\sqrt{2\pi\sigma_{\mathrm{k},LN}^2}} \exp\left[-\frac{(\log R - \mu_{\mathrm{k},LN})^2}{2\sigma_{\mathrm{k},LN}^2}\right], \qquad \mathrm{k} \in \{\mathrm{n}, \mathrm{p}\}, \tag{30}$$

with shape parameters $\mu_{\mathrm{k},LN} \in (-\infty, \infty)$, $\sigma_{\mathrm{k},LN} > 0$, related to the mean and variance via

$$\bar{R}_{\mathrm{k},a} = \exp(\mu_{\mathrm{k},LN} + \sigma_{\mathrm{k},LN}^2/2), \tag{31}$$

$$\sigma_{\mathrm{k},a}^2 = \exp(\sigma_{\mathrm{k},LN}^2 - 1)\exp(2\mu_{\mathrm{k},LN} + \sigma_{\mathrm{k},LN}^2), \tag{32}$$

Least-square fits of lognormals to the data, using the SciPy optimize package, are also shown in Fig. 2, and the distribution parameters (mean $\bar{R}_{\mathrm{k},a}$ and standard deviation $\sigma_{\mathrm{k},a}$) are given in Table 1. By our choice of distribution family, the result is one additional parameter per electrode, the area-weighted standard deviation $\sigma_{\mathrm{k},a}$, not present in the DFN.

Given the lognormal fits for $f_{\mathrm{k},a}(R_{\mathrm{k}})$ and the active material volume fraction $\epsilon_{\mathrm{s,k}}$ (taken from [18] unaltered), the total surface area per unit volume is then calculated via (19)—see [23]. Note that (19) is similar to that typically used in the literature for the DFN, where all particles are of a single radius, but with the appropriate single radius given by the area-weighted mean $\bar{R}_{\mathrm{k},a}$. In Chen et al. [18], the number-based mean particle radii were used, which are less than the fitted values of $\bar{R}_{\mathrm{k},a}$ as calculated here. Therefore, given the active material volume, [18] overestimates the surface areas compared to the true areas calculated using the PSD.

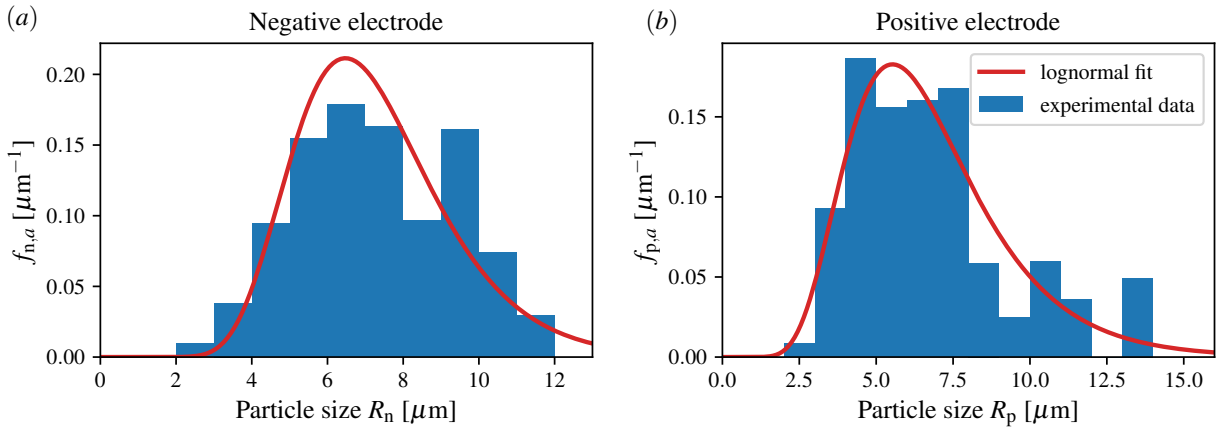

Figure 2: Experimental measurements and lognormal fits of area-weighted particle-size distributions $f_{\mathrm{k},a}(R_{\mathrm{k}})$, using data from Chen et al. [18]. (a) Negative electrode k = n (data for graphite only, SiO_x neglected); (b) Positive electrode k = p (NMC 811).

3.2 Other modified parameters

The determination of several parameters in the set provided in [18] relied on an estimate of the typical or single representative particle size for each electrode. These parameters include the reaction rates (m_{k}, k = n, p) and solid-state lithium diffusion coefficients ($D_{\mathrm{s,k}}$, k = n, p), determined via electrochemical impedance spectroscopy (EIS) and pulse galvanostatic intermittent titration technique (pulse GITT), respectively. Chen et al. [18] used the number-based mean radius, $\bar{R}_{\mathrm{k,num}}$, but here we choose the area-weighted mean radius, $\bar{R}_{\mathrm{k},a}$. As shown in Kirk et al. [23], a sphere of radius $\bar{R}_{\mathrm{k},a}$ exhibits precisely the same surface-area-to-volume ratio as the particle population. This mean radius is unique in this respect, and is therefore a much better choice to represent the PSD [23]. The aforementioned reaction rates[2] and diffusion coefficients based on $\bar{R}_{\mathrm{k,num}}$ can be readily updated so that they are instead based on $\bar{R}_{\mathrm{k},a}$ by a simple rescaling, and thus provide a consistent parameter set for the MP-DFN. The reaction rates m_{k} were determined from EIS data using Eqs (18) and (20) in [18], from which we find $m_{\mathrm{k}} \propto (a_{\mathrm{tot,k}})^{-1} \propto \bar{R}_{\mathrm{k},a}$. The diffusion coefficients $D_{\mathrm{s,k}}$ were determined using Eq. (14) in Chen et al., following GITT pulses (averaged across experiments at different states of charge, then later tuned for different C-rates), from which we observe $D_{\mathrm{s,k}} \propto (a_{\mathrm{tot,k}})^{-2} \propto (\bar{R}_{\mathrm{k},a})^2$. Hence, estimates based on the new radius can be found via the transformations

$$m_{\mathrm{k}} = \left(\frac{\bar{R}_{\mathrm{k},a}}{\bar{R}_{\mathrm{k,num}}}\right) m_{\mathrm{k}}^{\mathrm{Chen}}, \qquad D_{\mathrm{s,k}} = \left(\frac{\bar{R}_{\mathrm{k},a}}{\bar{R}_{\mathrm{k,num}}}\right)^2 D_{\mathrm{s,k}}^{\mathrm{Chen}}, \tag{33}$$

[2] In the PyBaMM implementation, the parameter that is rescaled in practice is the exchange current density $j_{0,\mathrm{k}}$.

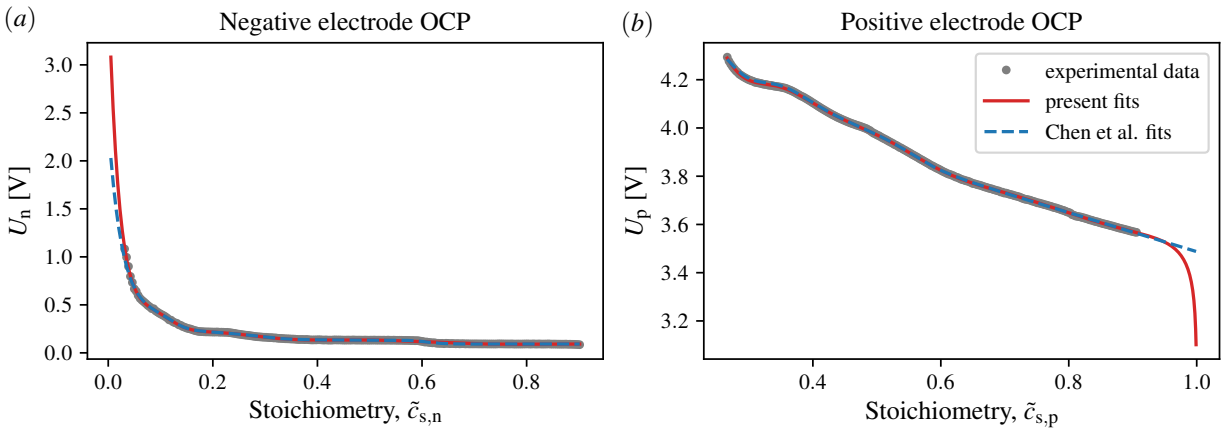

Figure 3: OCP analytical fits to OCP data from [18]. Shown are the fits from Chen et al. [18] (Eqs. 8 and 9 therein), and our fits (Eqs. (34) and (35)) that include logarithmic singularities at $\tilde{c}_{s,k} = 0, 1$. (a) Negative electrode k = n (graphite-SiO$_x$); (b) Positive electrode k = p (NMC 811).

where $\bar{R}_{k,a}/\bar{R}_{k,n} = 1.24, 1.30$ for k = n, p, and m_k^{Chen}, $D_{s,k}^{Chen}$ are the Chen et al. [18] estimates. The resulting new estimates are given in Table 1.

An important observation is that these updated parameter estimates are not just applicable to the MP-DFN, but also the DFN if the particle radius $\bar{R}_{k,a}$ is used. This is because the relevant timescales in the model—the diffusion timescales τ_k and reaction timescales $\tau_{r,k}$—are unchanged from Chen et al, which is expected since these are the quantities they directly measured experimentally. As a consequence, the dimensionless DFN model equations are the same for both parameter sets, the original set from [18] and our modified one, resulting in the same terminal voltage and current response.

Lastly, it was necessary to slightly modify the fitted functional forms of the OCPs, i.e. $U_k(\tilde{c}_{s,k})$ where $\tilde{c}_{s,k} = c_{s,k}/c_{k,max}$ is the stoichiometry. Analytical fits were preferable to interpolation of the OCP data of [18] for two reasons: (i) to reduce computation time given the high dimensionality and complexity of the MP-DFN; (ii) to reduce erratic behaviour in smaller particles due to experimental noise, as they are more sensitive to small deviations in the OCP. Chen et al. [18] provides smooth analytical fits, but they were insufficient for our purposes since the expected logarithmic singular behaviour of $U_k(\tilde{c}_{s,k})$ at electrode depletion and saturation ($\tilde{c}_{s,k} \to 0, 1$), preventing the stoichiometries going below zero or above one, was not accounted for in the functional forms. The lack of any singularity was an issue particularly in the positive electrode because the experimental data is only provided up to a stoichiometry of $\tilde{c}_{s,p} \approx 0.91$, with no visible indication of a singularity at $\tilde{c}_{s,p} = 1$. This range is sufficient for the DFN, since the stoichiometry in the particle of mean radius remains less than 0.91 for a discharge to the cut-off voltage of 2.5 V. However, in the MP-DFN, smaller particles lithiate (or delithiate) more quickly and reach stoichiometries much closer to 1 (or 0), where they are prevented from exceeding 1 (or 0) by the steep gradients in the OCP.

Therefore, we modified the analytical OCPs to include theoretical logarithmic terms consistent with the Butler–Volmer equation (20)-(22) with transfer coefficients of 1/2 (see e.g. [27]), and then refitted the functions to the OCP data (available in PyBaMM). The resulting fits, using the SciPy Optimize package, are given by

$$\begin{aligned} U_{\mathrm{n}}(c) = & \frac{1}{2}\frac{R_g T}{F}\log\left(\frac{1-c}{c}\right) + 3.5392\,\exp(-50.381c) - 0.13472 \\ & + 98.941\tanh[4.1465(c-0.33873)] + 102.43\tanh[3.8043(c-0.31895)] \\ & - 0.19988\tanh[22.515(c-0.11667)] - 200.87\tanh[3.9781(c-0.32969)], \end{aligned} \tag{34}$$

$$\begin{aligned} U_{\mathrm{p}}(c) = & 5\frac{R_g T}{F}\log\left(\frac{1-c}{c}\right) - 27.648\,c + 52.167 \\ & - 56.030\tanh[6.7733(c-0.53398)] + 57.409\tanh[6.7071(c-0.53334)] \\ & + 53.227\tanh[0.67406(c-1.6653)] + 0.49701\tanh[14.355(c-0.30713)], \end{aligned} \tag{35}$$

and are shown in Fig. 3. They accurately fit the experimental data over the stoichiometry range provided, with RMSEs of 4.19 mV and 1.48 mV, respectively, but they also exhibit the appropriate singular behaviour near $\tilde{c}_{\mathrm{s,n}} = 0$ (Fig. 3(a)) and $\tilde{c}_{\mathrm{s,p}} = 1$ (Fig. 3(b)). We remark that the singularity strength (numerical coefficient of the log) in (35) was increased from 1/2 to 5 in order to improve the robustness of the parameter fitting procedure of section (5), allowing a wider range of parameters (i.e., those far from optimal) to be explored without violating the stoichiometry limits during the simulations. The impact on the model behaviour at the resulting optimal parameters, however, was minimal.

4 Methodology

4.1 Numerical simulations

The PyBaMM [25] package was used for simulations of the DFN and MP-DFN models. PyBaMM is an open source software that can quickly and robustly solve a variety of continuum battery models in a modular or "plug and play" framework. The DFN model was already available in PyBaMM, but the MP-DFN was newly implemented for the present work. The implementation is currently available at [28] and will be included in a future release of PyBaMM. For the results presented here, we employed finite volume discretizations in each spatial domain, with 30 volumes in each particle, 20 volumes (or "size bins") in the particle-size dimensions, 20 volumes in each electrode and 20 volumes in the separator. Finer meshes (up to 50, 50, 80 and 80 volumes in the respective domains) were also considered but the difference from the results presented here were negligible. For the case of nonlinear solid-state diffusion considered in section 5.3, the number of volumes in the particles was increased to 150 to ensure the concentration profiles (containing regions with large gradients) were sufficiently resolved. The discretization results in a system of differential algebraic equations,

and the time integration was performed using the fast CasADi solver [29] (employing automatic differentiation and the SUNDIALS IDA [30] package for systems of DAEs written in C) which is conveniently interfaced directly from PyBaMM. In total, the MP-DFN system consisted of at least 24061 ordinary differential equations and 100 algebraic equations, and the absolute and relative tolerances of the solver were taken to be their default values of 10^{-6}. Each simulation of discharge plus relaxation took on the order of 40-50 s on a laptop computer with an Intel® Core i5-8350U CPU (1.70GHz × 8) and 16 GB RAM.

Regarding the particle-size dimensions R_{k}, particular to the present work, it was also numerically necessary to impose minimum and maximum particle radii, $R_{\mathrm{k,min}}$ and $R_{\mathrm{k,max}}$, for each electrode $\mathrm{k} = \mathrm{n}, \mathrm{p}$. We chose values based on the microscale parameters in Table 1 with $R_{\mathrm{k,min}} = 0.1\bar{R}_{\mathrm{k},a}$ and $R_{\mathrm{k,max}} = 6\bar{R}_{\mathrm{k},a}$ found to be sufficiently small and large (relative to the mean), respectively, giving $[R_{\mathrm{n,min}}, R_{\mathrm{n,max}}] = [0.728\,\mu\mathrm{m}, 43.68\,\mu\mathrm{m}]$ and $[R_{\mathrm{p,min}}, R_{\mathrm{p,max}}] = [0.678\,\mu\mathrm{m}, 40.68\,\mu\mathrm{m}]$. These values were kept fixed throughout the parameter fitting of section (5) where $\bar{R}_{\mathrm{k},a}$ and $\sigma_{\mathrm{k},a}$ were varied. The discretization then involved dividing these ranges into $N_{R,\mathrm{k}}$ equal-width volumes or bins, with $N_{R,\mathrm{k}} = 20$, $\mathrm{k} = \mathrm{n}, \mathrm{p}$ for the results shown here. We note that these reduced size ranges and the subsequent discretization necessitate the lognormal distributions (30), defined on the semi-infinite range $[0, \infty)$, to be renormalized and the internal parameters ($\mu_{\mathrm{k},LN}$,$\sigma_{\mathrm{k},LN}$) to be tweaked so that the distribution mean and variance are indeed the desired values (e.g., those in Table 1). This is to ensure that the relation (19) between $a_{\mathrm{tot,k}}$, $\bar{R}_{\mathrm{k},a}$ and $\epsilon_{\mathrm{s,k}}$ is preserved and thus the total active material volumes remain the experimentally determined values given in Table 1.

4.2 Experimental data

The experimental data that we compare our models to is the validation data taken from Chen et al. [18], consisting of constant current discharges from 100% state-of-charge until a cut-off voltage (2.5 V), followed by a relaxation period of 2 hours where no current is applied. (We refer to these here as discharge and relaxation experiments.) They considered experiments at three different C-rates, 0.5C, 1C, and 1.5C, where, for each C-rate, measurements were taken from three different cells to give a mean voltage, but also a standard deviation. All errors relative to experiment are measured relative to this mean voltage profile, but one standard deviation below and above are also shown in the figures, given by the thickness of the line. This gives some context to the size of the errors presented here, in comparison to the cell-to-cell variation.

4.3 Parameter fitting

Starting from the parameter set given in Table 1, the models were fitted to the experimental voltage data in a least-squares sense. For a given model (DFN or MP-DFN) and fitting parameters $\boldsymbol{\theta}$ (which depend on the model), the mean-squared error relative to the experimental

data is given by

$$\mathrm{MSE}_i(\boldsymbol{\theta}) = \frac{1}{N_i}\sum_{j=1}^{N_i}(V(t_j) - V_{\mathrm{data},j})^2, \tag{36}$$

where i corresponds to the experiment C-rate (0.5C, 1C or 1.5C), $V_{\mathrm{data},j}$ are the experimental data (at times t_j), and N_i is the number of data points. The objective or loss function that we choose to minimize is then the sum of the MSEs across all C-rates,

$$L(\boldsymbol{\theta}) = \sum_i \mathrm{MSE}_i(\boldsymbol{\theta}) = \mathrm{MSE}_{0.5}(\boldsymbol{\theta}) + \mathrm{MSE}_1(\boldsymbol{\theta}) + \mathrm{MSE}_{1.5}(\boldsymbol{\theta}). \tag{37}$$

We employ the mean-squared errors at each C-rate rather than just the squared error to account for the fact that the data at each C-rate are of different lengths. A meaningful measure of the error for each C-rate is given by the root-mean-squared error, $\mathrm{RMSE}_i = \sqrt{\mathrm{MSE}_i}$, and one across all C-rates is $\mathrm{RMSE}_{\mathrm{total}} = \sqrt{\frac{1}{3}\sum_i \mathrm{MSE}_i}$, which are used in Table 3.

The minimization was performed using the Derivative-Free Optimizer for Least Squares v1.0.2 (DFO-LS) [26]. DFO-LS is an open source robust nonlinear-least-squares minimizer for Python that does not require derivatives (i.e., the Jacobian) of the objective with respect to the parameters, and is designed for use with computationally expensive objective functions. This means it is well-suited to our purposes, where the evaluation of our objective function (37) requires the simulation of 3 discharge and relaxation experiments, taking up to 3 minutes in computation time. DFO-LS uses trust region methods [31] with the ability to impose bound constraints, excluding extreme or unphysical regions of the parameter space from the exploration. The parameter bounds used were conservative, e.g., with lower bounds of zero, and upper bounds of 5 times the initial guess (except for the diffusion coefficients, where no upper bounds were used). Doing this fitting required on the order of 50 function evaluations for convergence, with absolute and relative tolerances of 10^{-12} and 10^{-20}, respectively.

5 Results

In this section, we present modelling results that reproduce the experimentally observed slow relaxation of the voltage after a constant current discharge. First, the key aspects of the relaxation phenomenon are described, and then attempts to reproduce these aspects using the DFN model and the MP-DFN model are made, by fitting a relevant subset of parameters. Finally, to assess whether the use of a constant (Fickian) diffusion coefficient in the DFN model, rather than a single particle size, is responsible for the reported discrepancy with experiment, the DFN model employing nonlinear diffusion is considered.

5.1 Modelling the voltage relaxation

As discussed earlier, there are two key components of the voltage relaxation for a physical model to capture, which we repeat here: (i) The final equilibrium voltage after relaxation;

(ii) The shape or "speed" of the relaxation. We first elucidate the difficulties in consistently capturing the final voltage, particularly after a full discharge, and describe one remedy for this scenario, which we employ here. Then, we move on to the shape of the voltage relaxation.

5.1.1 Predicting the equilibrium voltage after relaxation

The equilibrium voltage after relaxation in our physical models is given simply by the OCV, $V_{\text{eq}} = U_{\text{p}}(\tilde{c}_{\text{s,p,eq}}) - U_{\text{n}}(\tilde{c}_{\text{s,n,eq}})$, where $\tilde{c}_{\text{s,p,eq}}$ and $\tilde{c}_{\text{s,n,eq}}$ are the final uniform stoichiometries in the positive and negative electrodes. Thus, predicting V_{eq} amounts to predicting $\tilde{c}_{\text{s,p,eq}}$ and $\tilde{c}_{\text{s,n,eq}}$. However, V_{eq} can depend very sensitively on these stoichiometries, particularly, close to 0% and 100% state-of-charge, where the OCPs, U_{p} and U_{n}, are singular with large gradients. Therefore, small errors in the model's internal states can result in significant errors in V_{eq}. This is not an issue if the experiment undertaken is a (dis)charge for a predefined length of time, when the final model stoichiometries are determined straightforwardly and accurrately via charge and lithium conservation, the only error being that made during electrode balancing. It is an issue, however, if the (dis)charge stopping criterion is a cut-off voltage close to 0% or 100% state-of-charge. This is evident in the model validations of, e.g., [14, 15, 16, 17, 19, 18], which include validation experiments of this type.

The experimental data which we consider here (see section 4.2) consist of constant current discharges from a fully-charged cell until the lower cut-off voltage of 2.5 V is reached, followed by 2 hours of relaxation. Fig. 4 shows the experimental data for a 0.5C discharge, and two numerical simulations of the DFN model, consisting of a 0.5C discharge: (i) until the cut-off voltage (2.5 V); (ii) for a specified amount of time, chosen to match the discharge time observed in the experiment. The DFN model is identical to the one in [18], which was validated by this data, and hence reasonably reproduces the discharge portion. If the cut-off voltage criterion is used, the model reaches this voltage slightly later ($\sim$ 102 s over a 2 hour discharge) compared to the experiment, resulting in a significant error in the final rest voltage. (In Chen et al. [18], the diffusion coefficient in the negative electrode was changed for each C-rate to alter the discharge time and hence reproduce the equilibrium voltage. This was motivated by the fact it is only an effective diffusion coefficient, representing transport in both the graphite and silicon components, and silicon is known to exhibit effects not included in the model, e.g. stress-enhanced diffusion [32].) However, the simulation with the specified discharge time, despite not reaching the cut-off voltage, captures the final rest voltage excellently. In fact, the experimental data (which is processed from raw data) was provided at approximately 5 second intervals, and hence the time until cut-off could only be extracted up to an error of ± 5 seconds. The time was then tweaked within this window to exactly fit the model to the final equilibrium voltage. Using the DFN, the discharge times for the 0.5C, 1C, 1.5C experiments were found to be 7084.80 s, 3544.56 s, 2360.23 s, respectively.

Even though the time-specified simulation does not reach the cut-off voltage, its peak error (see Fig. 4(b)), is comparable to the peak error of the simulation that does reach it. Furthermore, the times specified above are not just applicable to the DFN but also the MP-DFN, which we demonstrate in section 5.2. Therefore, for the fitting of the voltage relaxation

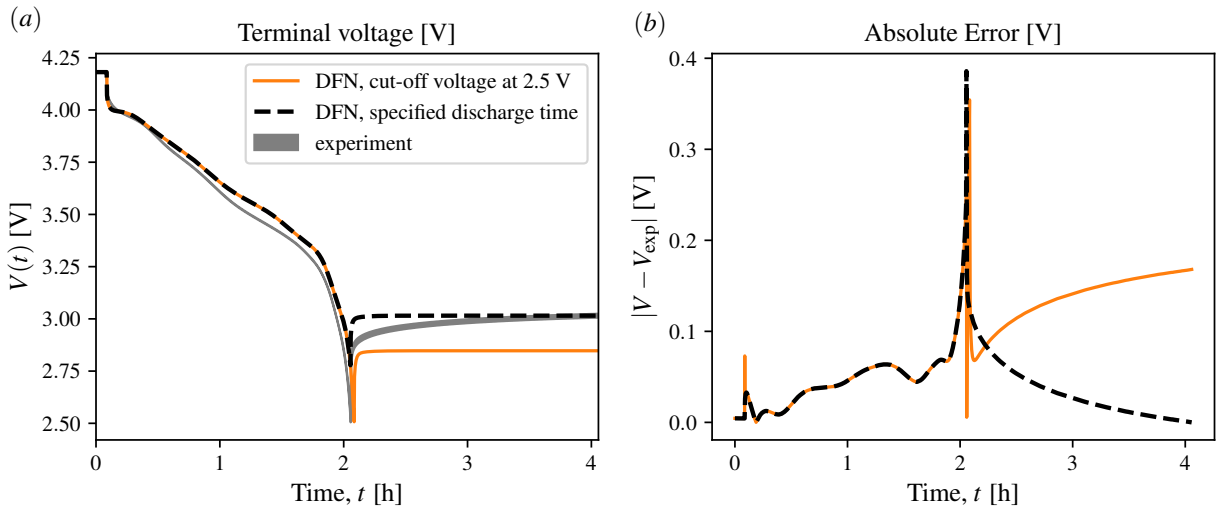

Figure 4: A discharge (0.5C) and relaxation, comparing two different DFN model simulations (section 2.3, parameters in Table 1) to experimental data of [18]. One simulation discharges until the cut-off voltage, 2.5 V, and the other for a specified time of 7084.80 s, matching the experimental time (to within approximately 5 s). Panel (a) shows the voltage, and (b) the absolute error of the simulations relative to the experiments.

shape in section 5.1.2 and 5.2, we fix the discharge times to be those above, ensuring the equilibrium voltage is not affected by the variation of the diffusion coefficients and electrode microstructure parameters. As we will see, the voltage at cut-off moves closer to 2.5 V naturally as the models are fit to the rest of the voltage curve.

5.1.2 Shape of the voltage relaxation

As observed in Fig. 4, and also other relaxation experiments in the literature [15, 17, 19], the voltage relaxes to the equilibrium value monotonically, but typically slower than seen in simulations. This implies an internal heterogeneity which equilibriates on a very long timescale (on the order of several hours) which does not seem to be present in the standard DFN-type model. The slowest timescale candidates in the DFN that may be responsible for this slow relaxation are the diffusion timescale of lithium in the electrode particles, and the reaction timescales, given by

$$\tau_{\mathrm{k}} = \frac{(\bar{R}_{\mathrm{k},a})^2}{D_{\mathrm{s,k}}}, \qquad \mathrm{k} = \mathrm{n}, \mathrm{p}, \tag{38}$$

$$\tau_{\mathrm{r,k}} = \frac{F}{m_{\mathrm{k}} a_{\mathrm{tot,k}} c_{\mathrm{e,typ}}^{1/2}} = \frac{F \bar{R}_{\mathrm{k},a}}{3 m_{\mathrm{k}} \epsilon_{\mathrm{s,k}} c_{\mathrm{e,typ}}^{1/2}}, \qquad \mathrm{k} = \mathrm{n}, \mathrm{p}. \tag{39}$$

These are timescales representative of the entire electrode(s). A model with a single particle size per electrode, such as the DFN, thus has a single diffusion timescale in each. For models

with many particle sizes (such as the MP-DFN), there is a diffusion timescale for each particle size, with those larger than the mean radius $\bar{R}_{\mathrm{k},a}$ having longer diffusion timescales, and therefore relaxations, than the mean particle. This distribution of diffusion timescales is one method of realistically including longer timescales in a physical model of the battery. We may vary the overall diffusion and reaction timescales (38)-(39) by varying $D_{\mathrm{s,k}}$ and $\bar{R}_{\mathrm{k},a}$, and control the spread of the distribution of timescales via the standard deviations $\sigma_{a,\mathrm{k}}$. In the next section we proceed to vary these microscale parameters in the DFN and MP-DFN models with emphasis on how they might influence reproducing the slow relaxation in the experiments.

5.2 Comparison of models and experiment

In this section, we directly compare the DFN and MP-DFN models to the experimental discharge and relaxation data (see section 4.2) across a range of C-rates. By varying the microscale parameters $D_{\mathrm{s,k}}$, $\bar{R}_{\mathrm{k},a}$, $\sigma_{a,\mathrm{k}}$, $\mathrm{k} = \mathrm{n}, \mathrm{p}$, best fits of the DFN and MP-DFN to the voltage profiles are presented and analyzed. The relevant parameter values, before and after fitting, are given in Table 2.

5.2.1 DFN model

First, to demonstrate that the DFN model (with a single particle size per electrode) cannot reproduce the slow relaxation phenomenon, we attempt a best fit to the experimental data, varying the four parameters $D_{\mathrm{s,k}}$, $\bar{R}_{\mathrm{k},a}$, $\mathrm{k} = \mathrm{n}, \mathrm{p}$. Although the parameter set in Table 1 is equivalent to the set in Chen et al. [18], and several parameters were already tuned by them to fit the DFN to this data, their fitting was done by hand using trial and error. Also, their diffusion coefficient in the negative electrode, $D_{\mathrm{s,n}}$, was made to depend on the C-rate in order to fit the final rest voltages. However, we take $D_{\mathrm{s,n}}$ to be independent of C-rate, and ensure the final rest voltages are accurate by fixing the cut-off times—see section 5.1.1. Therefore, to eliminate the possibility that the DFN can fit the slow relaxation with a better choice of parameter values, the fitting is performed here for all C-rate experiments simultaneously using a numerical optimization package—see section 4.3.

Fig. 5 shows the DFN results for the three discharge and relaxation experiments (0.5C, 1C, 1.5C), for the Chen et al. parameter set in Table 1, and after fitting. The voltages and the absolute error relative to the experiments are shown over time for each C-rate. Each simulation captures the final equilibrium voltage after relaxation since the discharge times have been specified to match these experimental data. Relative to the parameters from [18], $D_{\mathrm{s,n}}$ and $\bar{R}_{\mathrm{n},a}$ have been increased (τ_{n} decreased) in the fitted solution, and $D_{\mathrm{s,p}}$ and $\bar{R}_{\mathrm{p},a}$ have been decreased (τ_{p} increased). The fitting results in a modest improvement over the discharge portions for all C-rates, with $\mathrm{RMSE}_{\mathrm{total}}$ reduced from 42.2 mV to 37.1 mV—see Table 3. However, the relaxation portion is almost unchanged, with the speed of relaxation still greatly overestimated. Numerous different fits were attempted, employing different random seeds in the optimization and various parameter bounds, but no further improvement could be attained. It may be possible to reduce the relaxation speed (and

hence the error) of the DFN by fitting to only the relaxation portions but, as these results demonstrate, it does not appear possible while constrained to simultaneously fit the discharge portions.

5.2.2 MP-DFN model

We now present the results of the MP-DFN model compared to the experimental data, including the best fit under the variation of the six parameters $D_{\mathrm{s,k}}$, $\bar{R}_{\mathrm{k},a}$, $\sigma_{a,\mathrm{k}}$, $\mathrm{k} = \mathrm{n}, \mathrm{p}$. The same numerical optimization methods were used as the DFN, but now there are six fitting parameters rather than four. Fig. 6 shows the fitted MP-DFN results for the three discharge and relaxation experiments (0.5C, 1C, 1.5C), but also the best fit of the DFN for comparison. The MP-DFN shows an almost uniform reduction in error across all times and C-rates, compared to the best-fit DFN. Relative to the measured parameters (Table 2), $D_{\mathrm{s,n}}$ and $\bar{R}_{\mathrm{n},a}$ are increased (τ_{n} decreased) and $D_{\mathrm{s,p}}$ and $\bar{R}_{\mathrm{p},a}$ are decreased (τ_{p} increased), but the spreads of both particle-size distributions, $\sigma_{a,\mathrm{n}}$ and $\sigma_{a,\mathrm{p}}$, are increased—the fitted distributions can be seen in Fig. 7. The error during discharge portions is lower for the MP-DFN but, crucially, the relaxation has been slowed down to produce excellent fits to the experimental relaxations. As a result, the RMSE is reduced to 29.8 mV (0.5C), 12.3 mV (1C), 21.7 mV (1.5C), 22.4 mV (all C-rates), an approximately 40% overall error reduction relative to the best DFN fit.

The poor fit near the current cut-off for 0.5C is due to a slow voltage drop at the end of discharge. The fit can be improved considerably if we modify one parameter, $D_{\mathrm{s,n}}$ say, for this C-rate only. If this is done, the best-fit value for $D_{\mathrm{s,n}}$ is 1.30×10^{-13} $\mathrm{m^2 s^{-1}}$ and the agreement with experiment becomes remarkable, as shown in Fig. 9, with an RMSE of 10.3 mV. We remark that in the original parametrisation of Chen et al. [18], $D_{\mathrm{s,n}}$ had to be changed for each C-rate to correctly predict the rest voltage. (The fits in Fig. 9 are for $D_{\mathrm{s,n}}$ constant and independent of C-rate, with prediction of the rest voltage ensured by fixing the cut-off times.) Indeed, the negative electrode of these cells is actually composed of two active materials (silicon oxide in addition to graphite), and $D_{\mathrm{s,n}}$ is only an effective diffusion coefficient accounting for both in a single phase. Typical ranges for the diffusion coefficient (depending on the conditions and SoC) are $10^{-15} - 10^{-12}$ $\mathrm{m^2 s^{-1}}$ in graphite [33, 14, 16] and $10^{-16} - 10^{-13}$ $\mathrm{m^2 s^{-1}}$ in silicon oxide [34, 35], with the fitted effective values here, $D_{\mathrm{s,n}} = O(10^{-13})$, lying within these ranges. Indeed, it is remarkable that we could find such good agreement to the experiments with an effective diffusion coefficient.

The errors (RMSE) of each model (DFN and MP-DFN), for the parameters from [18] and our fitted parameters, are summarized in Fig. 8 and Table 3. The MP-DFN model, using either parameter set, exhibits smaller errors than the DFN (except for one case at 1.5C), and the fit MP-DFN model has the lowest error for any C-rate.

Finally, we comment on the differences between the fitted size distributions and those measured directly in [18]—both are shown in Fig. 7. Since the measurements are done on cross-sections of the electrodes (and therefore the active particles), one may expect the measured mean radii to underestimate the true mean, and indeed, the fitted mean for the

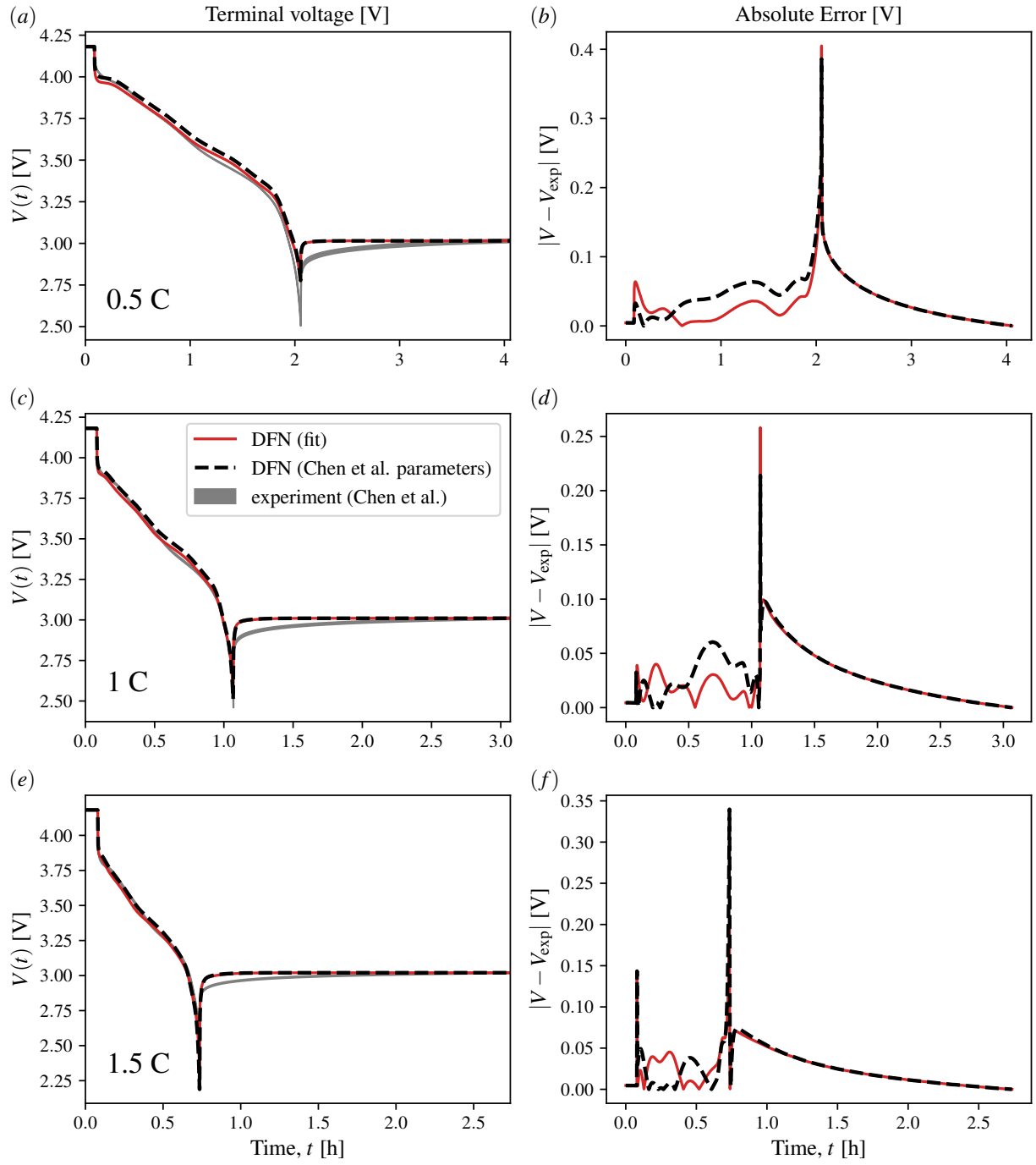

Figure 5: Comparison between discharge and relaxation experiments [18] and simulations of the DFN model (section 2.3), for parameter set from [18] (Table 1), and fitted parameters (Table 2). The rows correspond to different C-rates (0.5C, 1C, 1.5C), with the terminal voltage shown in the left column, and the error relative to experiment shown on the right. Width of experimental curve is 2 standard deviations (centred on the mean) measured from three cells (see section 4.2 or [18]).

Dimensional parameter	unit	Electrode $\mathrm{k} \in \{\mathrm{n}, \mathrm{p}\}$	From [18]	Fit	
			DFN/MP-DFN	DFN	MP-DFN
$D_{\mathrm{s,k}}$	$\mathrm{m^2 s^{-1}}$	n	5.10×10^{-14}	2.70×10^{-13}	5.25×10^{-13}
		p	6.75×10^{-15}	1.49×10^{-15}	1.76×10^{-14}
$\bar{R}_{\mathrm{k},a}$	m	n	7.28×10^{-6}	14.6×10^{-6}	9.98×10^{-6}
		p	6.78×10^{-6}	3.39×10^{-6}	4.10×10^{-6}
$\sigma_{a,\mathrm{k}}$	m	n	2.08×10^{-6}	-	6.15×10^{-6}
		p	2.59×10^{-6}	-	5.43×10^{-6}
$a_{\mathrm{tot,k}}$	$\mathrm{m^{-1}}$	n	3.09×10^{5}	1.55×10^{5}	2.26×10^{5}
		p	2.94×10^{5}	5.88×10^{5}	4.87×10^{5}

Table 2: Parameters from [18] (Table 1) and fitted parameter values corresponding to the fits of the DFN and MP-DFN models to the discharge and relaxation experimental data [18].

negative electrode is larger than the measured value. However, the difference in the mean for the positive electrode is more significant. The fitted mean is 40% lower than the measured value which, together with the larger variance, results in significantly more smaller particles, i.e., those around 1 μm or less. One explanation is that NMC811, the positive electrode active material, is known to form large secondary particle agglomerates ($\sim$1-15 μm) out of many smaller primary particles ($< 1\,\mu$m) [36]. From their SEM images, the particles measured by [18] may be the secondary agglomerates, based on their size. If so, our results suggest that the primary particle size should be used in physical models rather than the secondary one.

5.3 Nonlinear solid-state diffusion

In this paper, the focus has been on the impact of particle-size distributions on the relaxation phenomenon, and the impact of the lithium transport model within the active particles has not yet been discussed in detail. In particular, we have assumed Fickian diffusion, i.e., constant solid-state diffusivities $D_{\mathrm{s,k}}$, $\mathrm{k} = \mathrm{n}, \mathrm{p}$, which is known to be a considerable simplification, especially for graphite where phase-separation models are more appropriate. The measured diffusivities are typically strong functions of stoichiometry [14, 16], and this is also the case for the cells considered here, as reported in [18], but not implemented in their DFN model. As the transport model is expected to have a meaningful impact on the relaxation dynamics, the constant diffusivity approximation may be responsible for the discrepancy between the DFN model predictions and experiments, rather than particle-size distributions.

To explore this alternative explanation, we also considered a DFN model with nonlinear diffusion in the electrode particles, i.e., allowed the diffusivities to be functions of stoichiometry, $D_{\mathrm{s,k}} = D_{\mathrm{s,k}}(\tilde{c}_{\mathrm{s,k}})$, $\mathrm{k} = \mathrm{n}, \mathrm{p}$. We used diffusivity profiles based on the measurements of Chen et al. [18] (see Fig. 13(a) and 13(b) therein). We took a subset of approximately 20-30 repesentative data points for the diffusivity in each electrode, and then, to implement within PyBaMM, we used cubic spline interpolation on $\log[D_{\mathrm{s,k}}(\tilde{c}_{\mathrm{s,k}})]$. For the negative and posi-

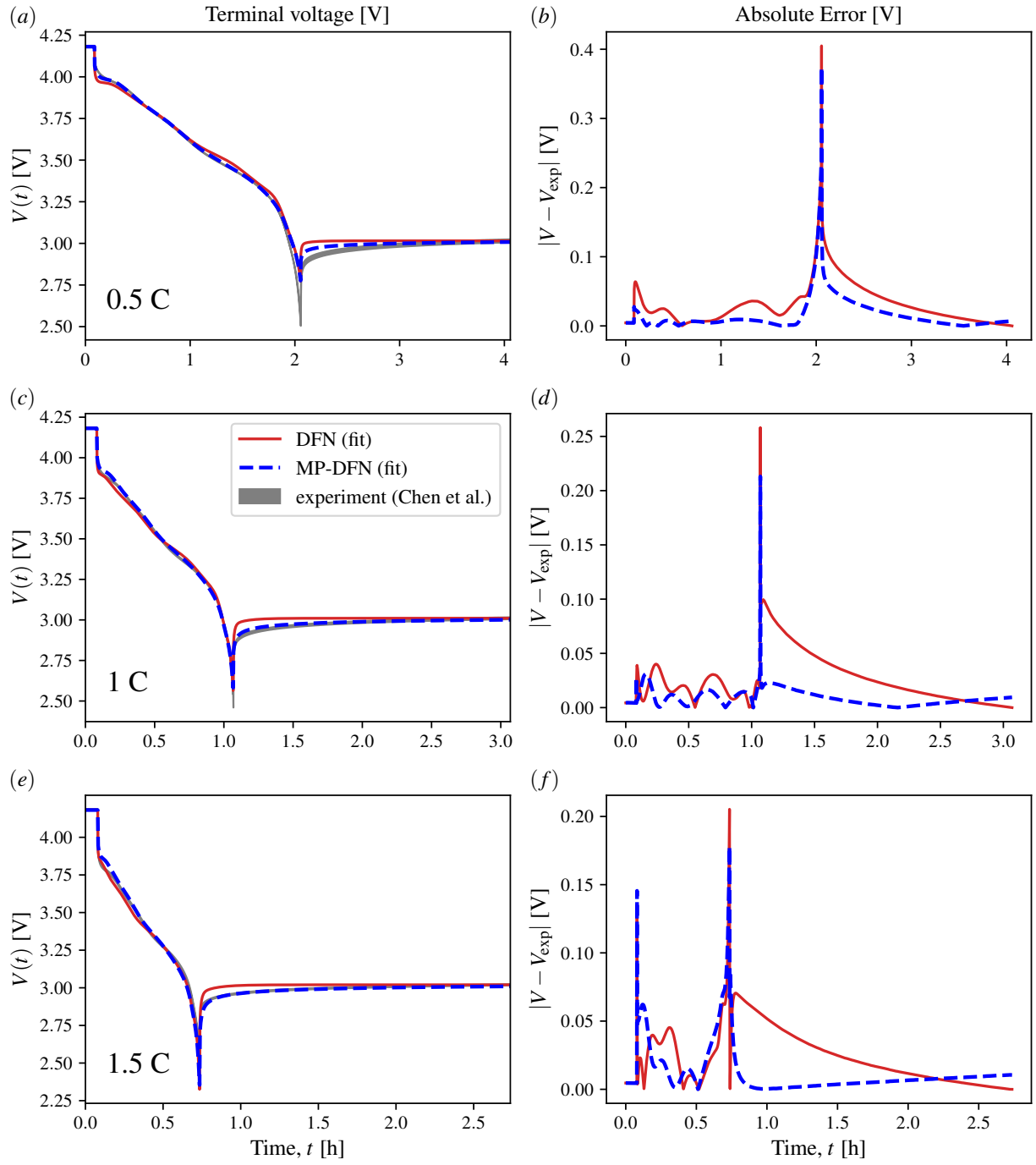

Figure 6: Comparison between discharge and relaxation experiments [18] and fitted simulations of the MP-DFN model (section 2). Also shown is the fitted DFN model, with fitted parameters in Table 2. The rows correspond to different C-rates (0.5C, 1C, 1.5C), with the terminal voltage shown in the left column, and the error relative to experiment shown on the right. Width of experimental curve is 2 standard deviations (centred on the mean) measured from three cells (see section 4.2 or [18]).

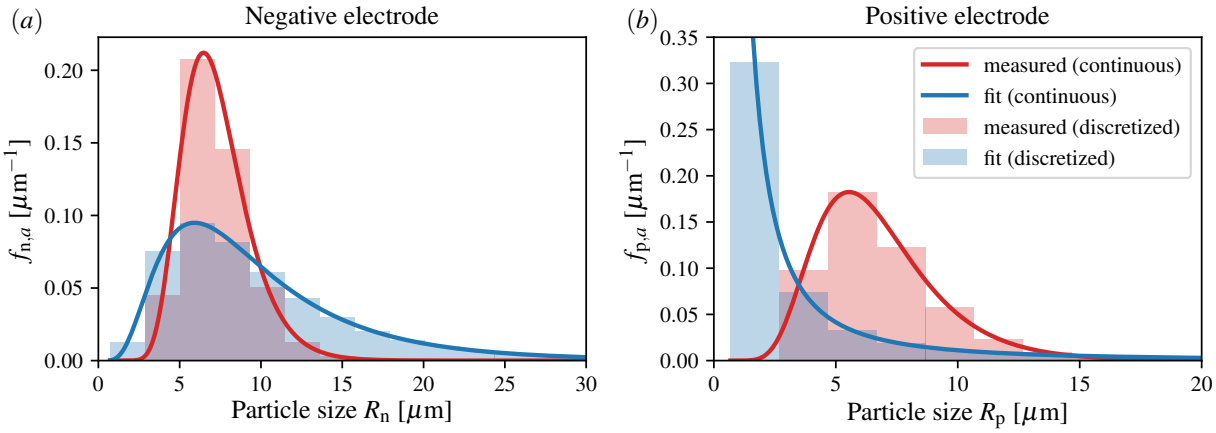

Figure 7: Area-weighted particle-size distributions $f_{\mathrm{k},a}(R_\mathrm{k})$, $\mathrm{k} = \mathrm{n}, \mathrm{p}$ from direct measurements [18] (red) and from fitting the MP-DFN model to voltage relaxation data (blue). The continuous lognormal densities are shown, as well as the discrete distributions that were employed in the PyBaMM simulations. For the means ($\bar{R}_{\mathrm{k},a}$) and standard deviations ($\sigma_{a,\mathrm{k}}$) see Table 2.

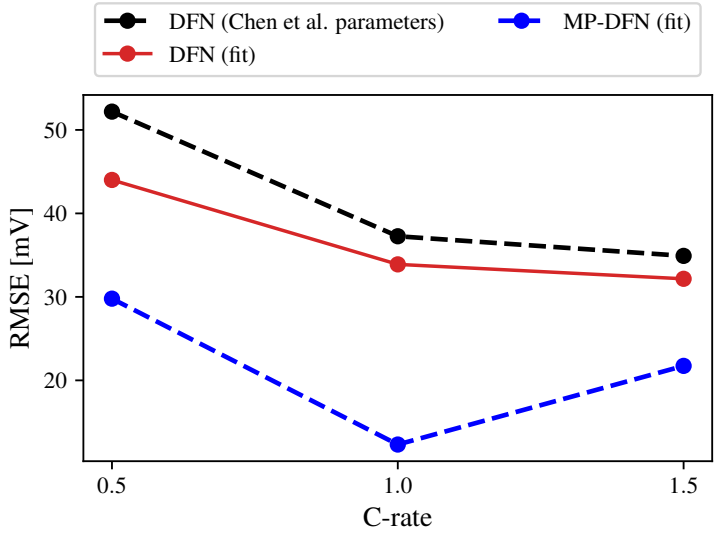

Figure 8: Root-mean-squared errors (RMSE) of the DFN and MP-DFN models relative to experimental data [18], for parameters from [18] (Table 1) and fitted parameters (Table 2). Errors are shown for the three different C-rates: 0.5C, 1C, 1.5C.

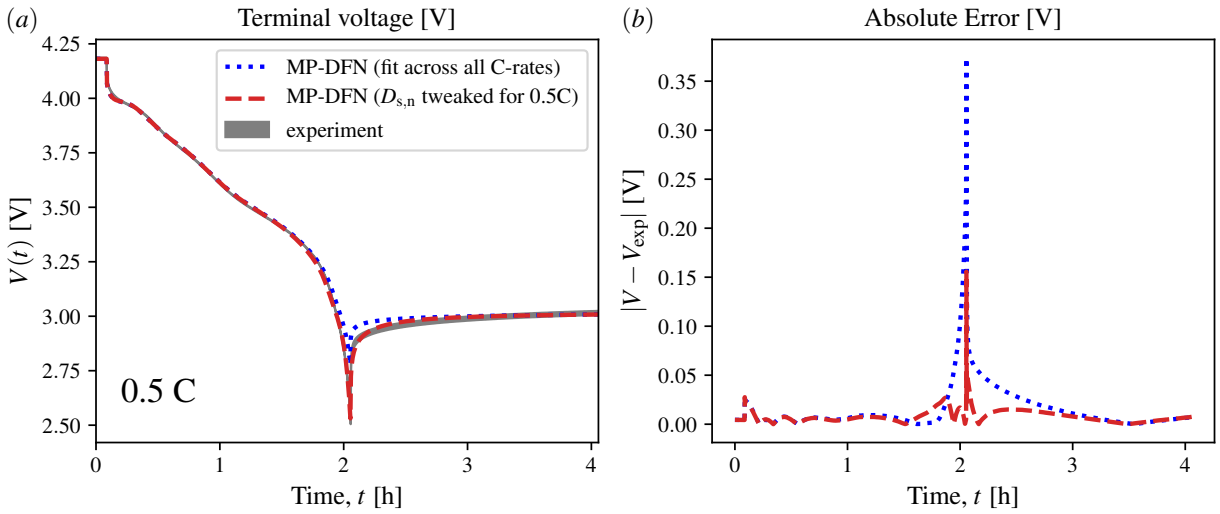

Figure 9: MP-DFN, with parameters fitted across all C-rates, and when $D_{s,n}$ is then tweaked for 0.5C only. Dotted line is for parameters in Table 2, and dashed line is the same but with $D_{s,n}$ changed to 1.30×10^{-13} m^2s^{-1} , giving RMSE of 10.3 mV, and cut-off voltage 2.531 V.

Quantity [unit]	Experiment	Parameter set			
		From [18]		Fit	
		DFN	MP-DFN	DFN	MP-DFN
Voltage RMSE [mV]	0.5C	52.2	37.8	44.0	29.8
	1C	37.3	25.2	33.9	12.3
	1.5C	34.9	54.7	32.2	21.7
	All C-rates	42.2	41.1	37.1	22.4
Voltage at cut-off [V]	0.5C	2.778	2.759	2.773	2.777
	1C	2.513	2.457	2.564	2.582
	1.5C	2.188	2.059	2.325	2.354

Table 3: Root-mean-squared errors (RMSE) of the DFN and MP-DFN models relative to experimental data [18], using parameters from [18] (see Table 1) and fitted parameters (Table 2). Also shown are the voltages just before current cut-off. Errors are shown for the three different C-rates: 0.5C, 1C, 1.5C, and RMSE across all C-rates calculated as in section 4.3. If $D_{s,n}$ is changed to $1.30 \times 10^{-13} m^2s^{-1}$ for 0.5C, MP-DFN (fit), then RMSE = 10.3 mV (0.5C), 15.6 mV (all C-rates).

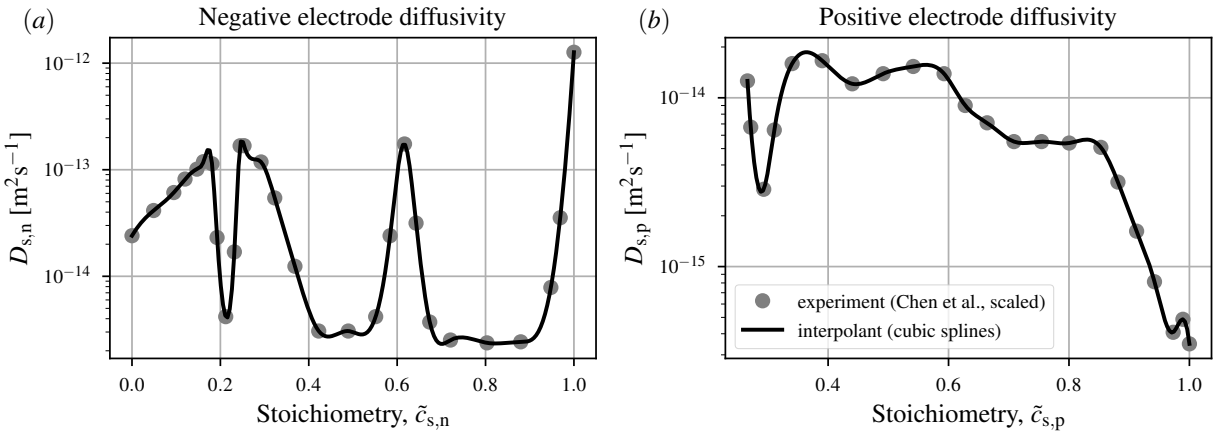

Figure 10: Solid-state diffusivities of Li as a function of stoichiometry in (a) the negative electrode, and (b) positive electrode. Circles are selected measurement from [18], modified according to (33), and then scaled by: (a) 13.84; and (b) 3.49. Solid lines are the cubic spline interpolants, implemented on $\log D_{s,k}$, $k = n, p$, that are used in the DFN simulations with nonlinear diffusion in Fig. 11.

tive electrodes, we used the delithiation and lithiation branches, with stoichiometry ranges $\tilde{c}_{s,n} \in [0, 1]$ and $\tilde{c}_{s,p} \in [0.2661, 1]$, respectively. The diffusivity data was also scaled via (33) to be based on our different choice of mean particle radius. However, we found the measured diffusivity values to be too small, leading to a discharge at any C-rate terminating (reaching voltage limits) significantly earlier (e.g. 15 min early for a 1C discharge) than the experiment. To make a meaningful comparison to the experiment and the other models in this paper, we chose to increase both diffusivities uniformly via a constant scale factor. This retains the shape of the diffusivity profiles, which vary by more than 2 orders of magnitude depending on stoichiometry, and represent, e.g., phase transitions in graphite. (Note that a significant increase from the measured (constant) diffusivity values was also necessary in [18], for similar reasons.) These scale factors were found by fitting to the 1C discharge and relaxation experimental data, i.e. minimizing MSE_1 in (36). As a result, $D_{s,n}(\tilde{c}_{s,n})$ was scaled by 13.84 and $D_{s,p}(\tilde{c}_{s,p})$ by 3.49, with the final profiles given in Fig. 10.

To elucidate the potential of nonlinear diffusion versus particle-size distributions as explanations for the slow voltage relaxation, we compare predictions from the DFN model with nonlinear diffusion to those from the DFN and MP-DFN models with Fickian (i.e. constant) diffusion, for a 1C discharge and relaxation—see Fig. 11. The nonlinear diffusion results use the diffusivities in Fig. 10, but otherwise the parameters are the same as those in Table 1. The models (DFN and MP-DFN) with Fickian diffusion use the fitted parameters from section 5.2. As Fig. 11 shows, the DFN model with nonlinear diffusion agrees with the experiment near the beginning and end of the discharge portion, but there are noticable differences to the DFN model with Fickian diffusion. Despite this clear impact of the diffusion model, the relaxation of both DFN models is almost identical, with the speed of relaxation

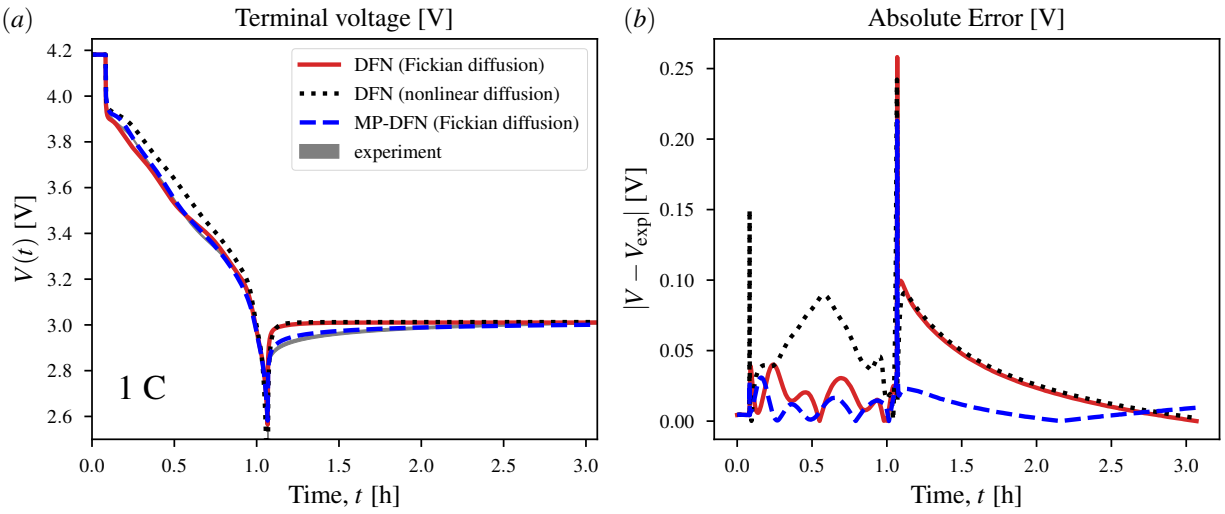

Figure 11: Comparison between the DFN with nonlinear solid-state diffusion (diffusivities in Fig. 10, parameters from Table 1), and the DFN and MP-DFN models with Fickian solid-state diffusion (constant diffusivities, fitted parameters from Table 2). Discharge at 1C and relaxation experimental data from [18]—see section 4.2.

overpredicted. The MP-DFN model, even though employing only Fickian diffusion here, is much closer to the experimental relaxation than either DFN model. (Note that the MP-DFN results are best fits across the three C-rates 0.5C, 1C, 1.5C, whereas the nonlinear diffusion DFN results were fit to the 1C data only.) This provides further evidence that, at least for the cells considered here, a particle-size distribution rather than nonlinear diffusion is more relevant to the accurate modelling of the relaxation. In addition, these results are in line with those of Ecker et al. [15] and Schmalstieg et al. [17] for other cell chemistries, which show discrepancies in relaxation speed between their model and experiment, despite the inclusion of nonlinear solid-state diffusion.

Further modifications to the diffusivity profiles (or other parameters) could be made to better match the experiments during discharge, but an approach that is physically motivated is not clear at present. Ultimately, models including particle-size distributions and non-Fickian transport should be considered, but they are outside the scope of this study.

6 Conclusions and Future Work

In this paper we explored, using physical models, the voltage relaxation phenomenon previously observed but not physically explained by several parametrization and modelling studies on lithium ion batteries. We focused on the discharge and relaxation experimental data of Chen et al. [18], taken from a set of commercial cells (LGM50, cylindrical 21700), wherein the relaxation after a full discharge was inadequately reproduced by the physical model they

considered: the Doyle–Fuller–Newman (DFN) model that is used extensively in the literature. This poor fitting of the DFN model is seen across numerous other parametrization studies.

Here we considered an extension of the DFN model to include a distribution of particle sizes in the active material of each electrode, rather than a single size as assumed in the DFN model. This model, denoted the Many-Particle-DFN (MP-DFN), was initially parametrized by modifying the DFN parameter set in [18] to include lognormal (area-weighted) particle-size distributions (PSDs) fitted to measurements taken (but not used) in [18]. This process of adapting an existing DFN parameter set for use with the MP-DFN is detailed, with attention given to numerical robustness and the use of physically relevant mean particle radii, in order to facilitate the process for other cells and chemistries.

The discharge and relaxation simulations of the MP-DFN model were then compared to the experimental data, and contrasted with those of the DFN model. To account for experimental uncertainty in the electrode microstructure properties, the PSDs (i.e., the mean radii and standard deviations) and effective diffusivity of lithium in the active material were also optimized to best fit the voltage data across the full range of C-rates (0.5C, 1C, 1.5C). The numerical simulations were performed using the flexible and robust software package PyBaMM, and the parameter optimization used a derivative-free nonlinear least squares minimizer, DFO-LS, written in Python.

The final equilibrium voltage after the relaxation period was able to be consistently captured, by both the MP-DFN and DFN models, by matching the discharge time to that observed in each experiment. We found that the DFN model always overestimates the speed of the voltage relaxation, even with parameter optimization, showing that a timescale of sufficient length is likely not possible within the model. However, our results show that the MP-DFN model can exhibit a relaxation slow enough to match that of the experiments, owing to a distribution of diffusion timescales and greater scope for internal heterogeneities. Even for the experimentally measured microstructure parameters, the MP-DFN model better matched the experiments during discharge as well as the relaxation. This can be greatly improved with parameter optimization, where the spread of the PSDs (and hence distribution of timescales) are increased, resulting in remarkable agreement for all C-rates, and an average error of 22.4 mV, or 15.6 mV if the diffusivity in the negative electrode is modified for one value of the C-rate (0.5C). Finally, we also considered nonlinear diffusion in the electrode particles as an alternative explanation for the slow relaxation. The DFN model results with nonlinear diffusion showed differences during discharge to the DFN model results with Fickian (constant) diffusion, but almost no improvement during relaxation. The MP-DFN model results agreed better with experiment than those from either DFN model, providing further evidence that, at least for the cells considered here, including a particle-size distribution rather than nonlinear diffusion is more relevant to the accurate modelling of the relaxation.

Avenues for future work include the consideration of lithium ion batteries with different electrode chemistries. The cells modelled here have negative electrodes that are a composite of two active materials (graphite and silicon oxide), but only one material was modelled for simplicity. Experiments on cells without composite electrodes, or models extended to

account for the composite explicitly, may allow even better agreement without necessitating that, e.g., diffusivities depend on the C-rate. One could also consider (dis)charge relaxation experiments with cut-offs chosen at other states of charge, far from 0% or 100% where the OCPs are steep, reducing the difficulties in capturing the equilibrium states. Finally, the MP-DFN is computationally expensive, which motivates deriving reduced-order models that can display the same behaviour—this is currently under way.

Acknowledgments

The authors acknowledge funding provided by The Faraday Institution, grant number EP/S003053/1, FIRG003. We thank the Energy Materials Group (University of Birmingham) and the Energy Group (University of Warwick) for providing the experimental data from Chen et al. [18]. We are also grateful to Robert Timms for helpful discussions on the numerical simulation of the MP-DFN model using PyBaMM.

A MP-DFN model: dimensionless governing equations

In this appendix we state the dimensionless variables and equations that are solved numerically in PyBaMM. We employ a dimensionless scheme similar to that of Marquis et al. [37], summarised in Table 5. Dimensional quantities are now indicated by an asterisk in this appendix to distinguish them from their dimensionless counterparts. The physically relevant timescales and resulting dimensionless parameters are given in Table 4. The dimensionless problem is summarised below.

Charge conservation

$$\frac{\partial i_{\mathrm{e,k}}}{\partial x} = \begin{cases} J_{\mathrm{k}}, & \mathrm{k} = \mathrm{n}, \mathrm{p}, \\ 0, & \mathrm{k} = \mathrm{sep}, \end{cases} \qquad \mathrm{k} \in \{\mathrm{n}, \mathrm{sep}, \mathrm{p}\}, \tag{40}$$

$$i_{\mathrm{s,k}} = i_{\mathrm{app}}(t) - i_{\mathrm{e,k}}, \qquad \mathrm{k} \in \{\mathrm{n}, \mathrm{p}\} \tag{41}$$

$$i_{\mathrm{e,k}} = \epsilon_{\mathrm{k}}^{b} \hat{\kappa}_{\mathrm{e}} \kappa_{\mathrm{e}}(c_{\mathrm{e,k}}) \left[-\frac{\partial \phi_{\mathrm{e,k}}}{\partial x} + 2(1 - t^{+}) \frac{\partial}{\partial x} \log c_{\mathrm{e,k}} \right], \qquad \mathrm{k} \in \{\mathrm{n}, \mathrm{sep}, \mathrm{p}\}, \tag{42}$$

$$i_{\mathrm{s,k}} = -\sigma_{\mathrm{k}} \frac{\partial \phi_{\mathrm{s,k}}}{\partial x}, \qquad \mathrm{k} \in \{\mathrm{n}, \mathrm{p}\}, \tag{43}$$

At $x = L_{\mathrm{n}}, 1 - L_{\mathrm{p}}$ there is continuity of $i_{\mathrm{e,k}}, \phi_{\mathrm{e,k}}$ and $i_{\mathrm{s,k}} = 0$, and at the current collectors,

$$i_{\mathrm{e,k}} = 0, \qquad \text{at } x = 0, 1 \tag{44}$$

$$i_{\mathrm{s,k}} = i_{\mathrm{app}}(t), \qquad \text{at } x = 0, 1 \tag{45}$$

$$\phi_{\mathrm{s,n}} = 0 \qquad \text{at } x = 0, \tag{46}$$

$$\phi_{\mathrm{s,p}} = V(t) \qquad \text{at } x = 1. \tag{47}$$

Parameter	Definition	Interpretation	Region k		
			n	sep	p
τ_{d}^*	$F^* c_{\mathrm{n,max}}^* L^* / i_{\mathrm{typ}}^*$	Discharge timescale		$1.10 \times 10^5 / \mathcal{C}$	
τ_{e}^*	$L^{*2} / D_{\mathrm{e,typ}}^*$	Diffusion timescale in the electrolyte		1.69×10^2	
τ_{k}^*	$(\bar{R}_{\mathrm{k},a}^*)^2 / D_{\mathrm{s,k}}^*$	Diffusion timescale in the average-sized electrode particle	1.04×10^3	-	6.81×10^3
$\tau_{\mathrm{r,k}}^*$	$F^* / (m_{\mathrm{k}}^* a_{\mathrm{tot,k}}^* (c_{\mathrm{e},0}^*)^{1/2})$	Reaction timescale in the electrode	1.23×10^4	-	2.34×10^3
$\mathcal{C}$	i_{typ}^* / C^*	C-rate		0.5, 1 or 1.5	
$\mathcal{C}_{\mathrm{k}}$	$\tau_{\mathrm{k}}^* / \tau_{\mathrm{d}}^*$	Ratio of solid diffusion to discharge timescales	$9.41 \times 10^{-3} \mathcal{C}$	-	$6.16 \times 10^{-2} \mathcal{C}$
$\mathcal{C}_{\mathrm{r,k}}$	$\tau_{\mathrm{r,k}}^* / \tau_{\mathrm{d}}^*$	Ratio of reaction to discharge timescales	$1.11 \times 10^{-1} \mathcal{C}$	-	$2.11 \times 10^{-2} \mathcal{C}$
L_{k}	L_{k}^* / L^*	Ratio of region thickness to cell thickness	0.493	6.94×10^{-2}	0.438
σ_{k}	$(R^* T^* / F^*) / (i_{\mathrm{typ}}^* L^* / \sigma_{\mathrm{k}}^*)$	Ratio of thermal voltage to the typical Ohmic drop in the solid	$6.39 \times 10^3 / \mathcal{C}$	-	$5.35 / \mathcal{C}$
$a_{\mathrm{tot,k}}$	$\bar{R}_{\mathrm{k},a}^* a_{\mathrm{tot,k}}^*$	Product of mean radius and active surface area per volume. (By choice of mean radius, this also corresponds to $3\epsilon_{\mathrm{s,k}}$.)	2.25	-	1.99
γ_{k}	$c_{\mathrm{k,max}}^* / c_{\mathrm{n,max}}^*$	Maximum lithium concentration in solid relative to maximum in negative electrode	1	-	1.90
$c_{\mathrm{k},0}$	$c_{\mathrm{k},0}^* / c_{\mathrm{k,max}}^*$	Initial stoichiometry in active material.	0.901	-	0.270
$\mathcal{C}_{\mathrm{e}}$	$\tau_{\mathrm{e}}^* / \tau_{\mathrm{d}}^*$	Ratio of electrolyte diffusion to discharge timescales		$1.53 \times 10^{-3} \mathcal{C}$	
γ_{e}	$c_{\mathrm{e},0}^* / c_{\mathrm{n,max}}^*$	Typical lithium concentration in electrolyte relative to maximum in negative electrode		3.02×10^{-2}	
$\hat{\kappa}_{\mathrm{e}}$	$(R^* T^* / F^*) / (i_{\mathrm{typ}}^* L^* / \kappa_{\mathrm{e,typ}}^*)$	Ratio of thermal voltage to the typical Ohmic drop in the electrolyte		$2.82 \times 10^1 / \mathcal{C}$	

Table 4: Dimensionless parameters and their definitions in terms of dimensional (asterisks) parameters. Dependence on the C-rate, denoted $\mathcal{C}$, is shown explicitly. When diffusion in electrode particles is nonlinear, $D_{\mathrm{s,k}}^*$ in the Table is replaced with $D_{\mathrm{s,k}}^*(1)$, the value at a stoichiometry of 1.

	Variable	Scaling	Description	Depends on coordinates	Regions k
Coordinates	t	t^*/τ_{d}^*	Time	-	-
	x	x^*/L^*	Distance from negative current collector	-	-
	R_{k}	$R_{\mathrm{k}}^*/\bar{R}_{\mathrm{k},a}^*$	Active particle radius	-	n, p
	r_{k}	$r_{\mathrm{k}}^*/R_{\mathrm{k}}^*$	Radial coordinate in active particle	-	n, p
Fundamental variables	$\phi_{\mathrm{s,k}}$	$(\phi_{\mathrm{s,k}}^* - \phi_{\mathrm{s,k}}^*\vert_{t^*=0})F^*/(R_g^*T^*)$	Electric potential in the solid	t, x	n, p
	$\phi_{\mathrm{e,k}}$	$(\phi_{\mathrm{e,k}}^* - \phi_{\mathrm{e,k}}^*\vert_{t^*=0})F^*/(R_g^*T^*)$	Electric potential in the electrolyte	t, x	n, sep, p
	$c_{\mathrm{s,k}}$	$c_{\mathrm{s,k}}^*/c_{\mathrm{k,max}}^*$	Lithium concentration in the active material	$t, x, R_{\mathrm{k}}, r_{\mathrm{k}}$	n, p
	$c_{\mathrm{e,k}}$	$c_{\mathrm{e,k}}^*/c_{\mathrm{e},0}^*$	Lithium-ion concentration in the electrolyte	t, x	n, sep, p
derived (known in terms of fundamental)	$i_{\mathrm{s,k}}$	$i_{\mathrm{s,k}}^*/i_{\mathrm{typ}}^*$	Current density in the solid	t, x	n, p
	$i_{\mathrm{e,k}}$	$i_{\mathrm{e,k}}^*/i_{\mathrm{typ}}^*$	Current density in the electrolyte	t, x	n, sep, p
	$N_{\mathrm{s,k}}$	$R_{\mathrm{k}}^*N_{\mathrm{s,k}}^*/(D_{\mathrm{s,k}}^*c_{\mathrm{k,max}}^*)$	Lithium flux in the active material	t, x	n, p
	$N_{\mathrm{e,k}}$	$L^*N_{\mathrm{e,k}}^*/(D_{\mathrm{e,typ}}^*c_{\mathrm{e},0}^*)$	Lithium-ion flux in the electrolyte	t, x	n, sep, p
	J_{k}	$J_{\mathrm{k}}^*L^*/i_{\mathrm{typ}}^*$	Total interfacial current density	t, x	n, p
	j_{k}	$j_{\mathrm{k}}^*a_{\mathrm{tot,k}}^*L^*/i_{\mathrm{typ}}^*$	Interfacial current density	t, x, R_{k}	n, p
	$j_{0,\mathrm{k}}$	$j_{0,\mathrm{k}}^*a_{\mathrm{tot,k}}^*L^*/i_{\mathrm{typ}}^*$	Interfacial exchange current density	t, x, R_{k}	n, p
	η_{k}	$F^*\eta_{\mathrm{k}}^*/(R_g^*T^*)$	Reaction overpotential	t, x, R_{k}	n, p
	U_{k}	$(U_{\mathrm{k}}^* - U_{\mathrm{k},0}^*)F^*/(R_g^*T^*)$	Open circuit potential	t, x, R_{k}	n, p
	$f_{\mathrm{k},a}$	$\bar{R}_{\mathrm{k},a}^*f_{\mathrm{k},a}^*$	Area-weighted particle-size distribution of active material (mean 1)	R_{k}	n, p
	D_{e}	$D_{\mathrm{e}}^*/D_{\mathrm{e,typ}}^*$	Lithium-ion diffusivity in the electrolyte	t, x	n, sep, p

Table 5: Dimensionless variables, the relations to their corresponding dimensional (asterisk) variable, and their regions of definition. The values correspond to the parameter set from [18], given in Table 1. When diffusion in electrode particles is nonlinear, $D_{\mathrm{s,k}}^*$ in the Table is replaced with $D_{\mathrm{s,k}}^*(1)$, the value at a stoichiometry of 1. The dimensionless diffusivity is then given by (54).

Molar conservation of lithium

$$\mathcal{C}_{\mathrm{e}}\gamma_{\mathrm{e}}\epsilon_{\mathrm{k}}\frac{\partial c_{\mathrm{e,k}}}{\partial t} = -\gamma_{\mathrm{e}}\frac{\partial N_{\mathrm{e,k}}}{\partial x} + \mathcal{C}_{\mathrm{e}}\frac{\partial i_{\mathrm{e,k}}}{\partial x}, \quad \mathrm{k} \in \{\mathrm{n}, \mathrm{sep}, \mathrm{p}\}, \tag{48}$$

$$N_{\mathrm{e,k}} = -\epsilon_{\mathrm{k}}^{b} D_{\mathrm{e}}(c_{\mathrm{e,k}})\frac{\partial c_{\mathrm{e,k}}}{\partial x} + \frac{\mathcal{C}_{\mathrm{e}} t^{+}}{\gamma_{\mathrm{e}}} i_{\mathrm{e,k}}, \quad \mathrm{k} \in \{\mathrm{n}, \mathrm{sep}, \mathrm{p}\}, \tag{49}$$

At $x = L_{\mathrm{n}}, 1 - L_{\mathrm{p}}$ there is continuity of $c_{\mathrm{e,k}}, N_{\mathrm{e,k}}$, and at $x = 0, 1$ there is no-flux, $N_{\mathrm{e,k}} = 0$.

$$\mathcal{C}_{\mathrm{k}} R_{\mathrm{k}}\frac{\partial c_{\mathrm{s,k}}}{\partial t} = -\frac{1}{r_{\mathrm{k}}^2}\frac{\partial}{\partial r_{\mathrm{k}}}(r_{\mathrm{k}}^2 N_{\mathrm{s,k}}), \quad \mathrm{k} \in \{\mathrm{n}, \mathrm{p}\}, \tag{50}$$

$$N_{\mathrm{s,k}} = -\frac{\partial c_{\mathrm{s,k}}}{\partial r_{\mathrm{k}}}, \quad \mathrm{k} \in \{\mathrm{n}, \mathrm{p}\}, \tag{51}$$

$$N_{\mathrm{s,k}} = 0, \quad \text{at } r_{\mathrm{k}} = 0, \qquad\qquad \frac{a_{\mathrm{k}}\gamma_{\mathrm{k}}}{\mathcal{C}_{\mathrm{k}} R_{\mathrm{k}}} N_{\mathrm{s,k}} = j_{\mathrm{k}}, \quad \text{at } r_{\mathrm{k}} = 1, \tag{52}$$

and

$$J_{\mathrm{k}} = \int_{\Omega_{\mathrm{k}}'} f_{\mathrm{k},a}(R_{\mathrm{k}}) j_{\mathrm{k}} \, \mathrm{d}R_{\mathrm{k}}, \qquad \mathrm{k} \in \{\mathrm{n}, \mathrm{p}\}. \tag{53}$$

When nonlinear solid-state diffusion in the particles is considered, a factor of $D_{\mathrm{s,k}}(c_{\mathrm{s,k}})$ is present on the right hand side of (51), where

$$D_{\mathrm{s,k}}(c_{\mathrm{s,k}}) = \frac{D_{\mathrm{s,k}}^{*}(c_{\mathrm{s,k}}^{*}/c_{\mathrm{k,max}}^{*})}{D_{\mathrm{s,k}}^{*}(1)}, \tag{54}$$

and $D_{\mathrm{s,k}}^{*}(c_{\mathrm{s,k}}^{*}/c_{\mathrm{k,max}}^{*})$ is the dimensional diffusivity given as a function of stoichiometry $c_{\mathrm{s,k}}^{*}/c_{\mathrm{k,max}}^{*}$.

Electrochemical reactions

At $r_{\mathrm{k}} = 1$,

$$j_{\mathrm{k}} = j_{\mathrm{k},0} \sinh\left(\frac{\eta_{\mathrm{k}}}{2}\right), \qquad \mathrm{k} \in \{\mathrm{n}, \mathrm{p}\}, \tag{55}$$

$$j_{0,\mathrm{k}} = \frac{\gamma_{\mathrm{k}}}{\mathcal{C}_{\mathrm{r,k}}}(c_{\mathrm{s,k}})^{1/2}(1 - c_{\mathrm{s,k}})^{1/2}(c_{\mathrm{e,k}})^{1/2}, \qquad \mathrm{k} \in \{\mathrm{n}, \mathrm{p}\}, \tag{56}$$

$$\eta_{\mathrm{k}} = \phi_{\mathrm{s,k}} - \phi_{\mathrm{e,k}} - U_{\mathrm{k}}(c_{\mathrm{s,k}}), \qquad \mathrm{k} \in \{\mathrm{n}, \mathrm{p}\}, \tag{57}$$

Initial conditions

At $t = 0$,

$$c_{\mathrm{s,k}} = c_{\mathrm{k},0}, \qquad \mathrm{k} \in \{\mathrm{n}, \mathrm{p}\}, \tag{58}$$

$$c_{\mathrm{e,k}} = 1, \qquad \mathrm{k} \in \{\mathrm{n}, \mathrm{sep}, \mathrm{p}\}, \tag{59}$$

and all other variables initially equal to zero.

References

[1] G. E. Blomgren. The development and future of lithium ion batteries. *Journal of The Electrochemical Society*, 164(1):A5019–A5025, 2017.

[2] G. Zubi, R. Dufo-López, M. Carvalho, and G. Pasaoglu. The lithium-ion battery: State of the art and future perspectives. *Renewable and Sustainable Energy Reviews*, 89(C):292–308, 2018.

[3] A. A. Franco. Multiscale modelling and numerical simulation of rechargeable lithium ion batteries: concepts, methods and challenges. *RSC Advances*, 3:13027–13058, 2013.

[4] V. Ramadesigan, P. W. C. Northrop, S. De, S. Santhanagopalan, R. D. Braatz, and V. R. Subramanian. Modeling and simulation of lithium-ion batteries from a systems engineering perspective. *Journal of The Electrochemical Society*, 159(3):R31–R45, 2012.

[5] M. Doyle, T. M. Fuller, and J. Newman. Modeling of galvanostatic charge and discharge of the lithium/polymer/insertion cell. *Journal of the Electrochemical Society*, 140(6):1526–1533, 1993.

[6] T. F. Fuller, M. Doyle, and J. Newman. Simulation and optimization of the dual lithium ion insertion cell. *Journal of The Electrochemical Society*, 141(1):1–10, 1994.

[7] K. E. Thomas, J. Newman, and R. M. Darling. *Mathematical Modeling of Lithium Batteries*, pages 345–392. Springer US, Boston, MA, 2002.

[8] J. Newman and K. E. Thomas-Alyea. *Electrochemical Systems*. John Wiley & Sons, 2012.

[9] G. Richardson, G. Denuault, and C. P. Please. Multiscale modelling and analysis of lithium-ion battery charge and discharge. *Journal of Engineering Mathematics*, 72(1):41–72, 2012.

[10] Michael A. Roscher and Dirk Uwe Sauer. Dynamic electric behavior and open-circuit-voltage modeling of lifepo4-based lithium ion secondary batteries. *Journal of Power Sources*, 196(1):331 – 336, 2011.

[11] An Li, Serge Pelissier, Pascal Venet, and Philippe Gyan. Fast characterization method for modeling battery relaxation voltage. *Batteries*, 2(2), 2016.

[12] Lei Pei, Tiansi Wang, Rengui Lu, and Chunbo Zhu. Development of a voltage relaxation model for rapid open-circuit voltage prediction in lithium-ion batteries. *Journal of Power Sources*, 253:412 – 418, 2014.

[13] M. Petzl and M. A. Danzer. Advancements in OCV measurement and analysis for lithium-ion batteries. *IEEE Transactions on Energy Conversion*, 28(3):675–681, 2013.

[14] Madeleine Ecker, Thi Kim Dung Tran, Philipp Dechent, Stefan Käbitz, Alexander Warnecke, and Dirk Uwe Sauer. Parameterization of a physico-chemical model of a lithium-ion battery: I. Determination of parameters. *Journal of The Electrochemical Society*, 162(9):A1836–A1848, 2015.

[15] Madeleine Ecker, Stefan Käbitz, Izaro Laresgoiti, and Dirk Uwe Sauer. Parameterization of a physico-chemical model of a lithium-ion battery: II. Model validation. *Journal of The Electrochemical Society*, 162(9):A1849–A1857, 2015.

[16] J. Schmalstieg, C. Rahe, M. Ecker, and D. U. Sauer. Full cell parameterization of a high-power lithium-ion battery for a physico-chemical model: Part I. physical and electrochemical parameters. *Journal of The Electrochemical Society*, 165(16):A3799–A3810, 2018.

[17] Johannes Schmalstieg and Dirk Uwe Sauer. Full cell parameterization of a high-power lithium-ion battery for a physico-chemical model: Part II. thermal parameters and validation. *Journal of The Electrochemical Society*, 165(16):A3811–A3819, 2018.

[18] Chang-Hui Chen, Ferran Brosa Planella, Kieran O'Regan, Dominika Gastol, W. Dhammika Widanage, and Emma Kendrick. Development of experimental techniques for parameterization of multi-scale lithium-ion battery models. *Journal of The Electrochemical Society*, 167(8):080534, may 2020.

[19] Valentin Sulzer, S. Jon Chapman, Colin P. Please, David A. Howey, and Charles W. Monroe. Faster lead-acid battery simulations from porous-electrode theory: Part II. asymptotic analysis. *Journal of The Electrochemical Society*, 166(12):A2372–A2382, 2019.

[20] M. Farkhondeh and C. Delacourt. Mathematical modeling of commercial LiFePO4 electrodes based on variable solid-state diffusivity. *Journal of The Electrochemical Society*, 159(2):A177–A192, 2011.

[21] J. P. Meyers, M. Doyle, R. M. Darling, and J. Newman. The impedance response of a porous electrode composed of intercalation particles. *Journal of The Electrochemical Society*, 147(8):2930–2940, 2000.

[22] J. Song and M. Z. Bazant. Effects of nanoparticle geometry and size distribution on diffusion impedance of battery electrodes. *Journal of The Electrochemical Society*, 160(1):A15–A24, 2013.

[23] Toby L. Kirk, Jack Evans, Colin P. Please, and S. Jonathan Chapman. Modelling electrode heterogeneity in lithium-ion batteries: unimodal and bimodal particle-size distributions. arXiv:2006.12208, 2020.

[24] F. Röder, S. Sonntag, D. Schröder, and U. Krewer. Simulating the impact of particle size distribution on the performance of graphite electrodes in lithium-ion batteries. *Energy Technology*, 4(12):1588–1597, 2016.

[25] Valentin Sulzer, Scott G Marquis, Robert Timms, Martin Robinson, and S. J Chapman. Python Battery Mathematical Modelling (PyBaMM). ECSarXiv, 2020.

[26] Coralia Cartis, Jan Fiala, Benjamin Marteau, and Lindon Roberts. Improving the flexibility and robustness of model-based derivative-free optimization solvers. *ACM Transactions on Mathematical Software*, 45(3), August 2019.

[27] Gregory L. Plett. *Battery Management Systems, Volume 1: Battery Modeling*. Artech House, 2015.

[28] T. L. Kirk. Psd models repository (pybamm fork). `https://github.com/tobykirk/PyBaMM/tree/add-PSD-models`, 2021.

[29] Joel A E Andersson, Joris Gillis, Greg Horn, James B Rawlings, and Moritz Diehl. CasADi – A software framework for nonlinear optimization and optimal control. *Mathematical Programming Computation*, 11(1):1–36, 2019.

[30] Alan C Hindmarsh, Peter N Brown, Keith E Grant, Steven L Lee, Radu Serban, Dan E Shumaker, and Carol S Woodward. SUNDIALS: Suite of nonlinear and differential/algebraic equation solvers. *ACM Transactions on Mathematical Software (TOMS)*, 31(3):363–396, 2005.

[31] A. R. Conn, N. I. M. Gould, and P. L. Toint. *Trust-Region Methods*. MPS-SIAM Series on Optimization. MPS/SIAM, 2000.

[32] Jie Pan, Qinglin Zhang, Juchuan Li, Matthew J. Beck, Xingcheng Xiao, and Yang-Tse Cheng. Effects of stress on lithium transport in amorphous silicon electrodes for lithium-ion batteries. *Nano Energy*, 13:192–199, 2015.

[33] Myounggu Park, Xiangchun Zhang, Myoungdo Chung, Gregory B. Less, and Ann Marie Sastry. A review of conduction phenomena in li-ion batteries. *Journal of Power Sources*, 195(24):7904–7929, 2010.

[34] Ke Pan, Feng Zou, Marcello Canova, Yu Zhu, and Jung-Hyun Kim. Systematic electrochemical characterizations of si and sio anodes for high-capacity li-ion batteries. *Journal of Power Sources*, 413:20–28, 2019.

[35] Jung-In Lee, Younghoon Ko, Myoungsoo Shin, Hyun-Kon Song, Nam-Soon Choi, Min Gyu Kim, and Soojin Park. High-performance silicon-based multicomponent battery anodes produced via synergistic coupling of multifunctional coating layers. *Energy Environ. Sci.*, 8:2075–2084, 2015.

[36] Thomas M. M. Heenan, Aaron Wade, Chun Tan, Julia E. Parker, Dorota Matras, Andrew S. Leach, James B. Robinson, Alice Llewellyn, Alexander Dimitrijevic, Rhodri Jervis, Paul D. Quinn, Dan J. L. Brett, and Paul R. Shearing. Identifying the origins of microstructural defects such as cracking within Ni-Rich NMC811 cathode particles for lithium-ion batteries. *Advanced Energy Materials*, 10(47):2002655, 2020.

[37] S. G. Marquis, V. Sulzer, R. Timms, C. P. Please, and S. J. Chapman. An asymptotic derivation of a single particle model with electrolyte. *Journal of The Electrochemical Society*, 166(15):A3693, 2019.